Enhanced rock weathering for improved smallholder farmer welfare: An at-scale case study for rice agriculture in India

Jacob S. Jordan[1], Tom M.D. Mills[1], Jonah Bernstein-Schalet[1], Rashmi Dikshit[2], Anikendra Das[2,†], Dilip Patidar[2], Robin Marlar Rajendran[2], Nilesh Kumar[2], Fiona Alder[1], Michael T. Thorpe[1,3], Shantanu Agarwal[1], Laurence Y. Yeung[1], Indra Sekhar Sen[4], Noah J. Planavsky[5,6], and David. J. Beerling[7]

[1]Mati Carbon PBC, Houston Texas, 77019 U.S.A.
[2]Mati Carbon India Private Limited, 11/11, Sarvapriya Vihar, New Delhi, Delhi 110017, India Hauz Khas
[3]University of Maryland NASA Goddard Space Flight Center and CRESST II, Greenbelt, Maryland 20771, U.S.A.
[4]Department of Earth Sciences, Indian Institute of Technology Kanpur, Kanpur, Uttar Pradesh 208016, India
[5]Yale Center for Natural Carbon Capture, Yale University, New Haven, Connecticut 06511, U.S.A.
[6]Department of Earth and Planetary Sciences, Yale University, New Haven, Connecticut 06511, U.S.A.
[7]Leverhulme Centre for Climate Change Mitigation, School of Biosciences, University of Sheffield S10 2TN, UK
[†]now at GFZ Helmholtz Centre for Geosciences, Telegrafenberg, 14473 Potsdam, Germany

Abstract

Smallholder farmers produce approximately one-third of the world's food supply, but face persistent challenges from soil degradation, limited access to affordable inputs and growing climate variability. Utilizing enhanced rock weathering (ERW) offers a pathway to address these constraints while generating durable carbon dioxide removal (CDR). Commercial-scale deployments by Mati Carbon during the 2024 summer monsoon rice growing season in Chhattisgarh, India applied basalt on over 2,000 acres (810 ha) farmed by more than 600 smallholders. Key agronomic findings from paired field measurements indicate a median yield increase of 22.9%, corresponding to estimated revenue gains of $303 per farmer, or approximately 20% of baseline household income. Inference via a simplified mass-balance model applied to soil geochemical data constrains the first-year weathering extent at $\tau = 0.27$ (68% CI: 0.14–0.39), yielding an initial CDR potential of 1.6 (0.8–2.3) tons CO_2 per acre (4.0 (2.1–5.7) t CO_2 ha^{-1}). Together, these results demonstrate that ERW can simultaneously deliver measurable livelihood benefits and climate mitigation under real-world smallholder conditions. Importantly, CDR generates monetizable carbon removal outcomes that are economically separate from on farm productivity gains, enabling climate finance to underwrite the costs of soil restoration without requiring farmer co investment. Combined measurement of CDR potential and yield response provides the empirical foundation for scaling ERW in smallholder systems. Establishing these outcomes demonstrates a replicable pathway for climate-financed agricultural development.

1 Introduction

Farmers who tend less than two total hectares (smallholder farmers, Lowder et al. (2016)), play a central role in global food systems. An estimated 500 million smallholder farmers produce approximately one third of the world's food supply (FAO and ITPS, 2015), underpinning food security for billions of people. Yet, smallholder agricultural systems are increasingly hampered by declining soil quality, rising agricultural input costs and growing exposure to climate risks (IPCC, 2007). Addressing these challenges has direct implications for food security, rural livelihoods and climate mitigation.

In particular, widespread soil degradation is increasingly becoming a challenge in smallholder agriculture. Many smallholder-managed soils are nutrient-depleted, acidic and low in organic matter, resulting in yields that are well

below agronomic potential (FAO and ITPS, 2015). Under comparable agroecological conditions, smallholder farmers often achieve only around half the productivity of larger, more capital intensive farms, reflecting the combined effects of biophysical soil constraints and limited access to affordable, sustainable soil fertility interventions (Tittonell and Giller, 2013). This productivity gap is further reinforced by a persistent fertilizer deficit, as smallholders apply substantially lower nutrient inputs than commercial farms due to binding constraints related to affordability, access, and risk exposure (World Bank, 2007; Mueller et al., 2012). It is compounded by a persistent fertilizer gap, because smallholders typically apply far lower rates of macro- and micronutrients than commercial farms due to cost, availability and risk constraints (Ricker-Gilbert, 2020). Declining soil productivity can indirectly drive land-use change as farmers expand cultivated area to offset low productivity (IPCC, 2007). The result is a reinforcing cycle of declining resilience, heightened economic vulnerability, and rising environmental costs.

There is growing evidence that practices that reduce soil acidity can address the productivity gap by improving soil function while increasing resilience to climate stress (Lal, 2015). However, pathways that can improve soil health and function often impose additional labor demands or rely on costly and logistically complex inputs (Feder et al., 1985; Jayne et al., 2019), placing further strain on already resource-constrained smallholder farming systems. Rather than reflecting a lack of technical viability, these constraints limit adoption by increasing the burden on smallholders who operate with narrow financial and operational margins. This challenge has motivated interest in agricultural interventions that can deliver soil restoration and productivity gains while minimizing additional costs and complexity for farmers (FAO, 2011).

Enhanced Rock Weathering (ERW) is a promising soil restoration approach, particularly in the Global South where climate conditions are conducive to accelerating weathering rates (Edwards et al., 2017) and there are oppportunites for equitable climate change mitigation (Tu et al., 2026). ERW can improve soil chemical properties, increase nutrient availability and neutralize soil acidity, resulting in nontrivial agricultural yield gains (Beerling et al., 2018). There are reports in bench- and field-scale studies of higher and more resilient crop yields following application of silicate rock (Castro and Crusciol, 2013; Crusciol et al., 2016). A point for crucial scaling potential is that ERW can be financed through its climate impact (Smith et al., 2019; Beerling et al., 2025). When pulverized silicate minerals are applied to agricultural or managed lands, they react with soil CO_2 over time, generating durable Carbon Dioxide Removal (CDR) that can be valorized (Hartmann et al., 2013; Beerling et al., 2020). In parallel, by lowering the embedded emissions of agricultural production (Ali et al., 2008) and positively affecting organic carbon stocks (Xu et al., 2025) ERW may also expand access to new, higher value markets for low or negative carbon emissions- and lower impact commodities linked to regenerative practices.

ERW agricultural interventions deliver durable CDR ($\geq$ 1,000 years) with significantly lower infrastructure barriers compared to other CDR verticals (Fuss et al., 2018; National Academies of Sciences, Engineering, and Medicine, 2019; Beerling et al., 2020). Upon dissolution, alkaline mineral feedstock can convert atmospheric carbon dioxide to bicarbonate (Renforth, 2019). An illustrative weathering reaction for augite, a pyroxene that acts as a major constituent building block of basalt, is

$$CO_2(aq) + H_2O \rightleftharpoons H_2CO_3 \tag{1a}$$

$$(Ca_xMg_yFe_z)(Mg_{y'}Fe_{z'})Si_2O_6 + 4H_2CO_3 \longrightarrow xCa^{2+} + (y+y')Mg^{2+} + (z+z')Fe^{2+} + 2SiO_2(am) + 4HCO_3^- . \tag{1b}$$

For augite, $0.4 \leq x \leq 0.9$, $x + y + z = 1$ and $y' + z' = 1$. The leftmost site as written in the formula for augite ($Ca_xMg_yFe_z$) represents a distorted octahedral coordination primarily occupied by calcium. This site can accept other large cations, predominantly alkaline earth or alkali elements. The other site ($Mg_{y'}Fe_{z'}$) represents a smaller octahedral coordination that preferentially accepts transition metals, primarily Mg^{2+} and Fe^{2+}. This site will often substitute other transition metals that are micronutrients for crops such as Zn^{2+} (for discussion see Section 5.1).

ERW deployments aim to facilitate reactions where aqueous CO_2(aq), via carbonic acid (H_2CO_3), is replaced with bicarbonate (HCO_3^-). The bicarbonate derived from the incipient point of rock weathering is then transported from agricultural fields to the ocean through groundwater and river networks where it may remain stably sequestered for thousands of years. By inspection of Equations (1a) and (1b), it is readily apparent that the net silicate weathering reaction has the potential to provide nutrients in the form of cations (in this example case,

Ca^{2+}, Mg^{2+} and Fe^{2+}) and plant-available amorphous silica, $SiO_2(am)$, a crucial nutrient for many grassy crops such as rice and an essential input for water-stressed cropping systems (Van Soest, 2006; Coskun et al., 2016). The above weathering chemistry demonstrates the potential for ERW to aide in smallholder farmers' climate resilience while also performing a CDR function that can be sold on voluntary and future compliance markets.

Growth of carbon markets has created the conditions for the commercialization of durable CDR, allowing ERW to move from experimental trials towards structured, investable deployments. In this context, large-scale ERW implementation can be understood as a first-of-a-kind, commercial scale model for how support from the Global North might interface with farming systems in the Global South, mediated by CDR markets. Support of ERW can create an opportunity for durable climate mitigation and agronomic benefits for smallholders.

To examine this opportunity, this work analyzes a commercial-scale ERW deployment undertaken during the Kharif 2024 (summer monsoon) rice growing season in central India. The study centers on ERW as a pathway to improve smallholder agricultural systems. The analysis also evaluates the extent to which carbon removal deployment translates into development-relevant outcomes at a smallholder farm-level. This work provides an estimation of in-field weathering rates for feedstock measured at rice paddies, which allows us to explore the long-term financial potential for ERW derived CDR credits to support climate resilience programs. Ultimately, this study provides an assessment of potential atmospheric carbon dioxide drawdown due to the ERW deployment, the resultant impacts on rice yields and implications for smallholder farmer incomes.

2 Kharif 2024 ERW deployment and study summary

Prior to the 2024 monsoon-fed rice cropping season (Kharif), Mati Carbon deployed basalt feedstock in the vicinity of a base location in the Gaurela-Pendra-Marwahi (GPM) district of Chhattisgarh, India. The full deployment encompassed 636 smallholder farmers across 36 villages, covering more than 8,000 individual rice paddies. Within this deployment, the analysis integrates multiple nested datasets, including paired plot-level yield measurements, farmer-reported yield surveys and a defined weathering study area spanning six rural villages in Chhattisgarh. A full deployment and summary and overview of the study is summarized in Table 1.

Table 1: Summary statistics for the full deployment and analysis subsets

	Full deployment	**Yield survey**†	**Weathering study area**
Farmers	636	594	174
Rice paddies	8,657	8,319	2,662
Villages	36	35	6
Basalt applied (t)	39,584	38,154	11,210
Area (ac)	2,188	2,103	620
Area (ha)	886	851	251
N, measurements	44*	594	128

*Direct yield measurements (3 x (1 x 1 m)^2 patches) on a subset of deployment-wide plots. †Surveys were taken from the general deployment population of farmers. Deployment average application rate, $\mathcal{A} = 18.1$ tons of feedstock per acre (44.7 t ha^{-1}).

The deployment area studied in this work lies in close proximity to the Deccan Traps, one of the world's largest and most accessible basalt formations (Subbarao, 1988; Beane et al., 1986; Duncan and Pyle, 1988; Mahoney et al., 2000). This geographical context provides favorable conditions for large-scale enhanced rock weathering deployment, particularly by minimizing transport-related emissions associated with mineral feedstock supply. Moreover, the high temperatures and monsoonal rains represent an ideal climatic setting for ERW (Hartmann et al., 2013; Kantola et al., 2017; Beerling et al., 2020; Baek et al., 2023; Boudinot et al., 2023). The deployment area is denoted on a contextual map in Figure 1a. The northern portion of the GPM deployment watershed drains into the Ganga River, while the southern watershed drains into the Mahanadi River (Figure 1 b). Both the Ganga and the Mahanadi Rivers discharge into the Bay of Bengal. The GPM deployment site lies on top of soils that are predominantly classified as Alfisols by the Indian Central Ground Water Board (CGWB) (Singh et al., 2006). Inceptisols and Ultisols are also reported by the CWGB in the region (Central Ground Water

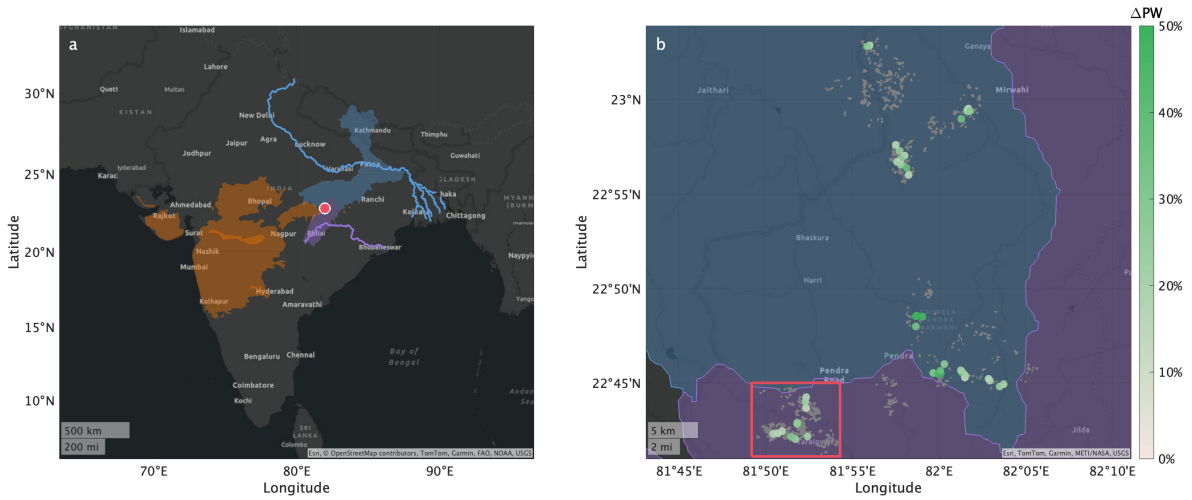

Figure 1: (a) Contextualized map of the Gaurela-Pendra-Marwahi (GPM) deployment location within India. The extent of the Deccan Traps flood basalt formation is highlighted in orange. The GPM deployment area drains into large rivers: the Ganga and the Mahanadi. The local watersheds that bisect the 2024 GPM deployment area are shaded blue–Ganga draining and purple–Mahanadi draining. The Ganga and Mahanadi rivers are highlighted in corresponding blue and purple. Both rivers terminate in the bay of Bengal. (b) A map showing the deployment shapes for individual rice paddies from the Kharif 2024 deployment at GPM. Scaled colorbar shows increase in paddy weight (%) discussed in Section 4.1. The local watersheds that drain into the Ganga and Mahanadi are shaded in blue and purple. Lastly, the weathering study area (Table 1) discussed in Section 4.2 is highlighted by a red boundary.

Board, North Central Chhattisgarh Region, 2023). These soils are developed atop dominantly felsic and mafic metamorphic material.

3 Methods

3.1 Rice yield impact estimation

Our analysis of rice yield from the 2024 Kharif ERW deployment uses paired plot yield measurements, which provide the primary evidence of treatment effects under controlled, field-based conditions. These measurements are complemented by large-scale farmer harvest surveys, which provide supporting evidence on system-wide performance, operational scalability and farmer-perceived outcomes.

3.1.1 Direct rice yield measurement

Direct rice yield measurements were conducted by Mati Carbon field staff at the time of harvest in collaboration with partner farmers ($n = 44$). Sampling was undertaken on paired, adjacent treatment (basalt applied) and control (business-as-usual) plots within the same farm, thereby controlling for farmer specific management practices, soil type and microclimatic conditions. Yield measurement followed a standardized quadrat harvesting protocol. A rigid square stencil with internal dimensions of 1 m $\times$ 1 m was placed within each rice paddy at random. All rice plants within the stencil were carefully harvested and the procedure was repeated at three locations per plot to account for within-field heterogeneity. Identical procedures were applied across treatment and control plots. Following harvest, plant material was air-dried and total biomass recorded. The rice was then threshed manually to separate grain from straw and the grain fraction weighed to determine paddy weight (PW). Plot-level yield responses were calculated as the proportional difference in paddy weight between paired treatment and control

plots (ΔPW, reported in %):

$$\Delta PW = \left[\frac{PW_{basalt} - PW_{control}}{PW_{control}} \right] \quad (2)$$

This paired-plot design isolates the causal effect of basalt application on yields by minimizing confounding factors from soil variability, management practices and weather-related factors. Aggregate results for the study area are presented in Figure 1b (See SI A).

3.1.2 Smallholder farmer survey for rice yield

To complement the direct yield measurements and assess performance across the broader deployment footprint, a structured Phase 4 harvest survey was administered to participating farmers ($n = 594$). These surveys provide supporting evidence on yield outcomes under operational conditions, capturing heterogeneity across agroecological zones, management practices and household contexts.

Enumerators verified farmer identity and plot selection prior to survey administration. Farmers were asked to report total harvested rice production per acre (0.405 ha) from basalt-treated land and separately, from a nearby non-treated control plot within the same holding, managed under comparable agronomic practices. The difference in reported production between deployed and non-deployed plots was recorded as the primary farmer-reported indicator of yield response. While farmer-reported yield data inherently contain greater measurement uncertainty than direct field sampling, they offer complementary insights into deployment-wide performance, farmer experience and system-level scalability (SI A.1).

3.2 Biomass characterization for rice

Rice grain and straw biomass samples analyzed in this study were collected from rice plants harvested during the direct yield measurements described in Section 3.1.1. Samples were processed in the Environmental Science department at the University of Nottingham. Samples were digested using an Anton Paar Multiwave microwave digestion system. Approximately 0.2 g of dry weight material was weighed into digestion vessels and combined with 3 mL concentrated HNO_3, 3 mL ultrapure (Milli-Q) H_2O, and 2 mL H_2O_2. The microwave digestion program consisted of three steps: (1) temperature ramp to 140°C over 10 min with stirrer off and fan level 1; (2) temperature hold at 140°C for 20 min with stirrer off and fan level 1; and (3) cooling to 55°C over 15 min with stirrer off and fan level 3. Following digestion, samples were diluted to a final volume of 20 mL.

Multi-element analysis of diluted solutions was undertaken by ICP-MS (Thermo-Fisher Scientific iCAP-Q; Thermo Fisher Scientific, Bremen, Germany). Samples were introduced (flow rate 1.2 mL min^{-1}) from an autosampler (Cetac ASX-520) incorporating an ASXpress™ rapid uptake module through a perfluoroalkoxy (PFA) Microflow PFA-ST nebuliser (Thermo Fisher Scientific, Bremen, Germany). Sample processing was undertaken using Qtegra™ software (Thermo-Fisher Scientific) utilizing external cross-calibration between pulse-counting and analogue detector modes when required.

The instrument was operated employing several operational modes. The iCAP-Q employs in-sample switching between two modes using a collision cell (i) charged with He gas with kinetic energy discrimination (KED) to remove polyatomic interferences and (ii) using H_2 gas as the cell gas. Typically, in-sample switching was used to measure Se in H_2-cell mode and all other elements in He-cell mode. Peak dwell times were 100 ms for most elements with 150 scans per sample. For each analysis, three internal repetitions were performed (RSD $< 2\%$).

Internal standards, used to correct for instrumental drift, were introduced to the sample stream on a separate line (equal flow rate) via the ASXpress unit or added directly to calibration standards and samples and introduced on a single line. Internal standards typically included combinations of Sc (10 µg L^{-1}), Ge (10 µg L^{-1}), Rh (5 µg L^{-1}), Re (5 µg L^{-1}) and Ir (5 µg L^{-1}). The matrices used for internal standards, calibration standards and sample diluents were typically either 2% Primar grade HNO_3 (Fisher Scientific, UK) with 4% methanol (to enhance ionization of some elements).

Calibration standards typically included (i) a multi-element solution with Ag, Al, As, Ba, Be, Cd, Ca, Co, Cr, Cs, Cu, Fe, K, Li, Mg, Mn, Mo, Na, Ni, P, Pb, Rb, S, Se, Sr, Ti, Tl, U, V and Zn, in the range 0–100 µg L^{-1}

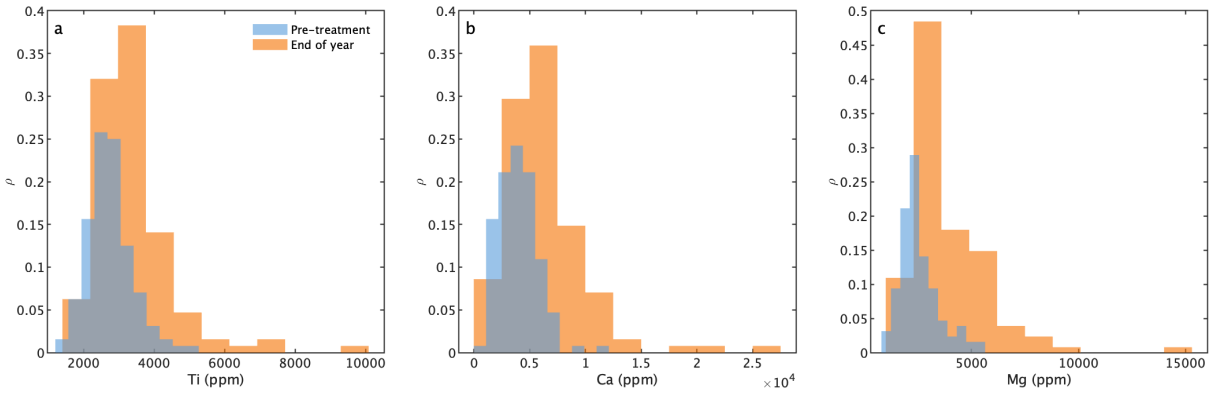

Figure 2: Raw, binned population-level compositional data (ppm) from the weathering study area. The presented data is from paired pre-treatment and end of year soil samples for (a) Ti, (b) Ca and (c) Mg ($n = 128$). The pre-treatment and end-of-year populations have a statistically robust difference in the immobile tracer, Ti ($p < 0.001$). By computing the difference $\Delta C = C_{post} - C_{pre}$ for each element at each location, the analysis isolates within-location changes due to basalt addition and weathering from background soil heterogeneity

(0, 20, 40, 100 µg L^{-1}) (Claritas-PPT grade CLMS-2 from SPEX Certiprep Inc., Metuchen, NJ, USA); (ii) a bespoke external multi-element calibration solution (PlasmaCAL, SCP Science, France) with Ca, Mg, Na and K in the range 0–30 mg L^{-1}; and (iii) a mixed phosphorus, boron and sulphur standard made in-house from salt solutions (KH_2PO_4, K_2SO_4 and H_3BO_3).

3.3 Soil and basalt feedstock analysis

Samples for analyzing the major and trace element concentration of elements in soil are collected prior to feedstock deployment. One year after feedstock deployment, a new set of soil samples were collected at the geotagged location of the pre-application soil sample. The elemental concentrations of sampled soils were directly measured using inductively -coupled-plasma optical-emission spectroscopy, ICP-OES, (for major-element concentrations in soil and feedstock) and inductively coupled plasma mass spectrometry, ICP-MS, (for trace-element concentrations). These measurements were conducted at a private analytical laboratory in Bengaluru, India: Shiva Analyticals. All samples (feedstock and soil) are prepared using a 4-acid digestion (HF, HNO_3, $HClO_4$ and HCl) and compositional measurements are conducted using the same analytical methods. Titanium was digested using a Na_2O_2 fusion method. All sample batches were analyzed with the certified reference material OREAS 231. Analytical error for Ti, Ca and Mg is $< 3\%$ across all batches (see SI A). With these three sets of compositional data, the framework for quantifying basalt weathering mixed into soil as described in Reershemius et al. (2023) can be applied. Pre-treatment and end-of-year soils (Figure 2) are considered pair-wise samples in the quantitative framework presented below. This paired-sample design is similar to a randomized complete block design where each sampling location serves as its own block such that each removes between-location variability from the error and increases statistical power (Snedecor and Cochran, 1989; Zar, 2010). By computing the difference $\Delta C = C_{post} - C_{pre}$ for each element at each location, the analysis isolates within-location changes due to basalt addition and weathering from background soil heterogeneity. Basalt from eight individual quarries was applied at the Kharif 2024 study site examined in this study.

3.4 Estimated CDR potential for Kharif 2024

CDR potential quantifies the mass of atmospheric CO_2 that can be durably removed through silicate weathering. Here we define CDR potential as the product of three terms: the alkalinity potential of the feedstock, E_{pot}, the

application rate, $\mathcal{A}$, and the extent of weathering, τ. To estimate CDR potential, we require compositional data for both the basalt feedstock and the amended soil, along with paired pre- and post-deployment soil measurements. Control plots (unamended soil) establish baseline elemental concentrations, enabling detection of weathering-derived cation loss against background soil heterogeneity.

The potential drawdown of CO_2, with units of kilograms drawdown per ton of deployment for alkaline feedstocks, is calculated after Renforth (2019) as

$$E_{\text{pot}} = \frac{M_{CO_2}}{100}\left(\alpha\,\frac{\text{CaO}}{M_{\text{CaO}}} + \beta\,\frac{\text{MgO}}{M_{\text{MgO}}} + \varepsilon\,\frac{\text{Na}_2\text{O}}{M_{\text{Na}_2\text{O}}} + \theta\,\frac{\text{K}_2\text{O}}{M_{\text{K}_2\text{O}}} + \gamma\,\frac{\text{SO}_3}{M_{\text{SO}_3}} + \delta\,\frac{\text{P}_2\text{O}_5}{M_{\text{P}_2\text{O}_5}}\right) 10^3\,\eta. \tag{3}$$

Oxide concentrations are in weight percent, M_i is the molar mass of each oxide and $\eta = 2$ reflects the stoichiometry of silicate weathering (2 mol CO_2 per mol divalent cation). The prefactors α, β, ε and θ are set to $+1$ for the base cations (Ca^{2+}, Mg^{2+}, Na^{+}, K^{+}), while γ and δ are set to -1 to correct for cations bound to sulfate and phosphate rather than bicarbonate.

The extent of feedstock weathering, τ, is a mass fraction bound on the interval $[0,\ 1]$ where $\tau = 1$ represents complete dissolution. We estimate τ from paired soil geochemical measurements using the mass-balance approach described below. Net geochemical CDR is then calculated as

$$\text{CDR}_{\text{net}} = E_{\text{pot}} \times \mathcal{A} \times \tau \times (1 - L), \tag{4}$$

where L represents fractional losses from downstream processes including secondary carbonate precipitation, riverine outgassing, and marine re-equilibration (see SI C). The initial CDR potential reported in this work corresponds to $L = 0$, representing gross CDR prior to transport and geochemical deductions.

The resulting CDR estimates for the study area are based on 128 treatment rice paddies and 31 control paddies (see area highlighted by red box in Figure 1b). To calculate the extent of feedstock weathering after deployment, we follow the conceptual models of Reershemius et al. (2023) and Suhrhoff et al. (2025). This framework conforms to current CDR crediting standards (Beerling et al., 2025). A detailed derivation of the forward model and sensitivity analysis is provided in SI B. To account for the heterogeneity in basalt sourcing, we compute a deployment-weighted average basalt composition for the study area (see SI A.3).

3.4.1 Quantitative framework for in-field feedstock weathering estimates: τ

The post-deployment soil within the study area is modeled as a mixture of three endmembers. They are:

1. The pre-application composition of the original soil, s
2. The pre-application composition of unweathered basalt feedstock as applied, b
3. The weathered residue of the basalt feedstock after cation leaching, w.

In this context, we define r to denote the initial mass fraction of rock in the amended soil. The extent of weathering τ is thus defined,

$$\tau = \frac{f_w}{f_b + f_w} = \frac{f_w}{r} \tag{5}$$

where f_w and f_b are the mass fractions of the weathered residue and basalt in post-deployment soil, respectively. The soil mass fraction for a given sampled soil, f_s, is typically much greater than f_w and f_b, ($f_s \gtrsim 0.9$). These mass fractions are non-negative and sum to unity and therefore lie on the unit simplex (i.e. $f_s + f_b + f_w = 1$).

We construct a forward model that first considers an immobile element, I and a mobile element, X, initially present in the basalt and soil. The equations

$$\Delta I = r\,(I_b - I_s), \tag{6a}$$
$$\Delta X = r\,(1 - \tau)(X_b - X_s), \tag{6b}$$

state that the immobile element associated with applied feedstock is added to the soil according to the basalt- and soil-endmember concentrations and r, while mobile elements are subject to an additional loss characterized by τ. All concentrations are unitless mass ratios like r. In this work, we take $I = \mathrm{Ti}$ and principally focus on $X \in \{\mathrm{Ca}, \mathrm{Mg}\}$. Here, $\Delta X = X^{\mathrm{post}} - X^{\mathrm{pre}}$ is the observed change in element X taken from paired soil samples (Pre-treatment and end of year populations). This simplified forward model is based upon the previously published work of Reershemius et al. (2023). Works such as Suhrhoff et al. (2025) have also explore the implications of the simplified mass balance framework described above. The outcome of making various model assumptions within similar mass-balance frameworks are discussed in SI B.

We define $\theta = \{\Delta\mathrm{Ti}_{\mathrm{obs}}, \Delta\mathrm{Ca}_{\mathrm{obs}}, \Delta\mathrm{Mg}_{\mathrm{obs}}\}$ to denote the observed mean element changes from the soil samples across the pre-deployment and end-of-year populations. At each of n sample locations, we measure element concentrations across the year-long trial period. This exercise yields paired differences in concentration $\Delta\mathcal{E}_i = \mathcal{E}_i^{\mathrm{post}} - \mathcal{E}_i^{\mathrm{pre}}$, for element i. The observed mean estimates the population mean change. By the Central Limit Theorem, the sampling distribution of this mean is approximately Gaussian. Therefore, we model the likelihood as

$$\mathcal{L}(\theta \mid r, \tau) = \mathcal{L}_{\mathrm{Ti}} \cdot \mathcal{L}_{\mathrm{Ca}} \cdot \mathcal{L}_{\mathrm{Mg}}, \tag{7}$$

where

$$\mathcal{L}_{\mathcal{E}} = \exp\left(-\frac{(\Delta\mathcal{E}_{\mathrm{obs}} - \Delta\mathcal{E}_{\mathrm{pred}})^2}{2\sigma_{\mathcal{E}}^2}\right). \tag{8}$$

Here, $\mathcal{E} \in \{\mathrm{Ti}, \mathrm{Ca}, \mathrm{Mg}\}$ and $\sigma_{\mathcal{E}} = \mathrm{SE}(\Delta\mathcal{E}) = s_{\mathcal{E}}/\sqrt{n}$ the standard error of the mean.

We use uninformative priors for the rock application rate and the extent of feedstock weathering so

$$p(r) \propto 1 \quad \text{for } r > 0 \tag{9a}$$
$$p(\tau) \propto 1 \quad \text{for } \tau \in [0, 1] \tag{9b}$$

Here, the posterior is computed on a grid spanning $r \in [0.0156, 0.1560]$, which was chosen to cover the region of non-negligible posterior density (i.e. elsewhere $p \sim 0$, see Figure 5a). The joint posterior is given

$$p(r, \tau \mid \theta) \propto \mathcal{L}(\theta \mid r, \tau) \cdot p(r) \cdot p(\tau). \tag{10}$$

The joint posterior $p(r, \tau \mid \theta)$ is shown in Figure 5a. While the joint distribution captures the full inferential uncertainty, reporting credible intervals for individual parameters requires marginalization. The marginal posteriors are obtained by integrating over the other parameter:

$$p(r \mid \theta) = \int_0^1 p(r, \tau \mid \theta)\, d\tau, \tag{11a}$$
$$p(\tau \mid \theta) = \int_0^\infty p(r, \tau \mid \theta)\, dr. \tag{11b}$$

These marginal distributions (Figure 5b,c) represent the uncertainty in each parameter after properly accounting for all uncertainty in the other. For example, the marginal $p(\tau \mid \theta)$ incorporates the full range of plausible r values, weighted by their posterior probability. Figure 5a also displays conditional distributions: $p(r \mid \tau, \theta)$ and $p(\tau \mid r, \theta)$, evaluated at the median values of each parameter. These conditional slices through the joint posterior are narrower than the corresponding marginals because they condition on a fixed value rather than integrating over uncertainty. The differences demonstrate the correlation structure between r and τ. Higher rock fractions are associated with higher weathering extents for a given observed cation loss. Credible intervals reported in this work are derived from the marginal posteriors. Marginalizing over nuisance parameters to report uncertainty in quantities of interest (Gelman et al., 2013; Berger, 1985) returns reported intervals for τ fully propagate uncertainty in r, rather than conditioning on a point estimate.

4 Results

4.1 Rice yield, plant- and soil-health outcomes with farmer revenue implications

Paired field measurements indicate higher rice yields in basalt-amended plots relative to adjacent control plots managed under business-as-usual practices. Across all paired observations ($n = 44$), paddy weight was consistently greater in treatment plots than in controls. As summarized in Table 2, the median proportional increase in paddy

Table 2: Yield changes and estimated net income from basalt application.

		Measured ΔPW		
	Yield change (%)	Yield change (Q ac^{-1})	(kg ha^{-1})	Net added income
Q25	17.5%	2.6	640	₹19,422 ($231)
Median	22.9%	3.4	840	₹25,510 ($303)
Q75	30.9%	4.6	1130	₹34,708 ($413)
N, measurements		44		
p-value		<0.001		

Net income per farmer after deducting incremental transport and packaging costs associated with the yield increase. Gross added income assumes rice was purchased at the 2024 government Minimum Support Price, MSP (₹2,250/quintal): gross income $= A \times Y_b \times \Delta\text{PW} \times MSP$, where mean landholding $A = 3.44$ acres and baseline yield $Y_b = 14.74\,\text{Q ac}^{-1}$. Incremental transport cost estimated using a proportional payload allocation model: trip cost $= d \times c \times 2$ (backhaul factor), where $d = 20$ km (Itin-Shwartz, 2026), $c = |35\,\text{km}^{-1}$ for a 5 t truck (NITI Aayog, 2021), yielding ₹280 t^{-1}; applied to median incremental yield of 1.16 t gives ₹325 per farmer. Additional packaging uses government benchmark of ₹10.22 per 50 kg bag (Government of India, 2025); 23.2 bags × ₹10.22 = ₹237. Total deduction: ₹562 ($6.68). Exchange rate: 84.12 INR/USD (31 October 2024). $p = 1.25\text{e}{-15}$ (one-sample t-test, $H_0: \Delta PW = 0$).

weight derived from measured treatment control pairs was 22.9%, with an inter-quartile range of 17.5–30.9%. Yield differences between treatment and control plots were statistically robust ($p < 0.001$). The lower quartile of observed yield increases remained positive, indicating that yield gains were not driven by a small number of high-performing plots. Measured yield outcomes were derived from contemporaneous treatment control pairs harvested within the same cropping period, reducing the influence of seasonal variability and enabling direct comparison under comparable field conditions. The dispersion in measured yield responses reflects heterogeneity across farms, soil conditions and management practices within the deployment area.

We use the prevailing government minimum support prices rice during the 2024 Kharif season to show that the measured yield increases correspond to meaningful gains in farmer revenue. Across the inter-quartile range of measured outcomes, estimated added revenue per farmer ranges from approximately $231 at the 25th percentile to $413 at the 75th percentile, with a median increase of approximately $303 (Table 2). These values represent gross revenue uplifts derived directly from measured agronomic yield changes and prevailing price assumptions. If the median proportional increase of 22.9% were to be realized across a comparable share of rice area within the subregion with similar agroecological characteristics, this would imply a material uplift in aggregate paddy production relative to business-as-usual baselines. Even under more conservative assumptions aligned with the 25th percentile estimate (17.5%), subregional rice output would be expected to increase meaningfully, given the extensive prevalence of similar soil constraints across the deployment landscape.

The farmer-reported survey outcomes are directionally consistent with measured results, reinforcing the external relevance of the paired-plot findings while acknowledging that survey data capture perceived rather than strictly measured yield changes (See SI A.1). The inter-quartile range of yield improvement as self-reported by the farmers would result in income gains of ∼$100-250 for an average landholding in the deployment. Together, the measured and self-reported evidence suggests that basalt amendment anecdotally delivered local yield improvements. Low-intensity forms of monitoring such as farmer surveys could be further developed across similar farming systems for expanded deployment.

The observed yield improvements can be attributed in part to the nutrient release associated with basalt

weathering. At the application rate of 44.7 t ha^{-1}, weathering is calculated to have released macro-inorganic nutrients including 861 kg ha^{-1} of calcium and 453 kg ha^{-1} of magnesium, alongside 27 kg ha^{-1} of potassium. For context, the potassium release (27 kg K ha^{-1}) represents approximately 50% of the recommended K_2O application rate for wetland rice in India (40–60 kg K_2O ha^{-1}), while the phosphorus release (10 kg P ha^{-1}) is comparable to a modest P fertilizer application (Dobermann and Fairhurst, 2000; Timsina et al., 2021) (see Table 3). The direct uptake of these macronutrients and the implications for CDR are briefly explored in SI C.2. Silicon release was 2,666 kg ha^{-1}. This represents a significant source of an essential element for rice cultivation that is frequently depleted in intensively cropped tropical soils (Savant et al., 1997). Among micronutrients, basalt weathering contributed iron (1,301 kg ha^{-1}), manganese (20 kg ha^{-1}), zinc (1.7 kg ha^{-1}), and copper (2.9 kg ha^{-1}). Deficiencies in these elements commonly constrain rice productivity in weathered tropical soils (Dobermann and Fairhurst, 2000; Shukla et al., 2021).

Table 3: Plant nutrient release from basalt weathering. Calculated based on inferred weathering and basalt chemistry ($\tau = 0.27$ and application rate of 44.7 t ha^{-1})

Element	Basalt (ppm)	Mass released		Moles released	
		(kg ha^{-1})	(kg ac^{-1})	(mol ha^{-1})	(mol ac^{-1})
Macronutrients					
P	857	10.37	4.20	334.9	135.5
K	2197	26.59	10.76	680.1	275.2
Ca	71098	860.59	348.27	21472.9	8689.8
Mg	37393	452.61	183.17	18622.3	7536.2
S	246	2.97	1.20	92.7	37.5
Si	220230	2665.72	1078.78	94912.9	38409.9
Micronutrients					
Fe	107502	1301.23	526.59	23300.7	9429.5
Zn	137	1.66	0.67	25.4	10.3
Mn	1617	19.57	7.92	356.2	144.2
Cu	243	2.94	1.19	46.2	18.7

Figure 3 presents preliminary data on elemental concentrations in rice grains ($n = 16$, 8 pairs) and straw biomass ($n = 6$, 3 pairs) from paired basalt-treated and control plots. The measurements are contextualized in the weathering study area (Figure 3a) originally presented in Figure 1. For major plant nutrients (Figure 3b), concentrations in both seed and biomass from basalt-treated plots remained within the range of variability observed in controls, with no systematic enrichment or depletion. Biomass showed somewhat greater variability than grain for several elements (Na, Mg, K), suggesting that grain filling may buffer against soil compositional changes more effectively than vegetative tissue accumulation. For potentially toxic elements (PTEs) (Figure 3c), arsenic, chromium, cadmium, copper, and nickel concentrations in basalt-treated samples were not systematically elevated relative to controls. Cadmium showed the largest apparent variability, but this reflected high variance in the control biomass rather than enrichment in treated plots.

Soil PTE concentrations showed no systematic enrichment following basalt application (Figure 4). Concentrations of cobalt, chromium, copper, niobium, nickel, lead, thorium, uranium, vanadium, and zinc in end-of-year samples remained within the range of variability observed in pre-application baseline samples. Chromium and vanadium, which are typically enriched in mafic lithologies, showed no significant increase despite the high application rate (44.7 t ha^{-1}). These observations are consistent with field trials in the US Corn Belt, where basalt amendment at comparable rates did not result in detectable PTE accumulation (Beerling et al., 2024). The absence of short-term PTE enrichment in both plant tissue and soil provides preliminary assurance for the environmental safety of single-season basalt application, though longer-term monitoring remains essential to evaluate cumulative effects under the repeated deployment of basalt amendments (e.g. Levy et al., 2024).

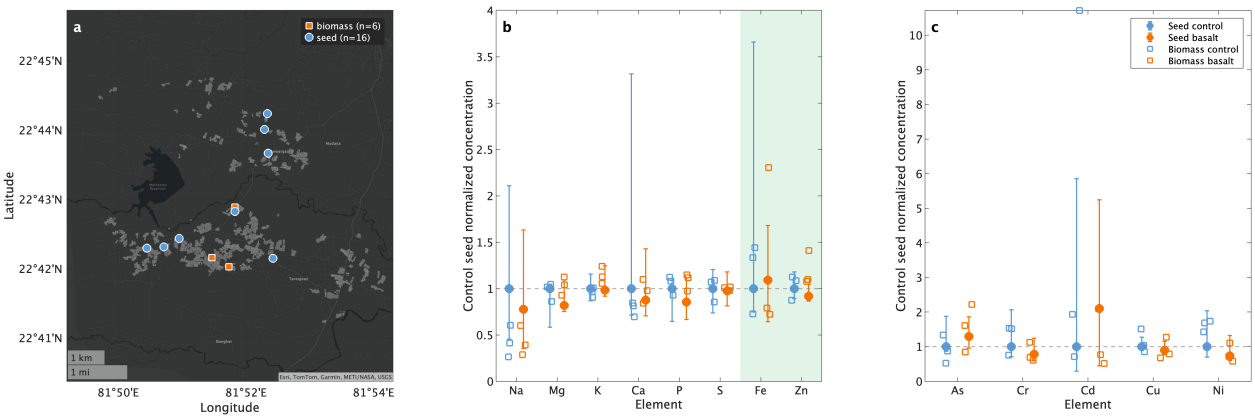

Figure 3: Elemental concentrations in rice grain and straw biomass from basalt-treated and control plots. (a) Sampling locations within the weathering study area showing biomass collection sites ($n = 6$, 3 pairs) and grain collection sites ($n = 16$, 8 pairs). (b) Major plant nutrient concentrations normalized to control grain values; green shading highlights elements (Fe, Zn). (c) Potentially toxic element concentrations normalized to control grain values. In both panels, filled symbols represent grain and open symbols represent biomass. Blue symbols indicates control plots and orange indicates basalt-treated plots. Error bars show the 68% confidence interval. Concentrations near unity indicate no systematic difference from controls.

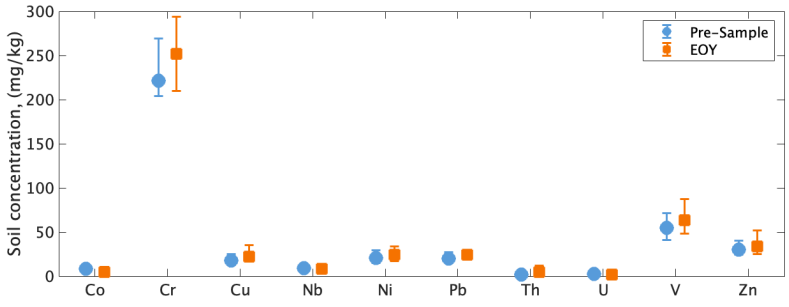

Figure 4: Potentially toxic element concentrations in soil before basalt application (Pre-Sample) and at end of year (EOY) following the 2024 Kharif season. Error bars show standard deviation. No significant enrichment of PTEs was observed following basalt amendment at 44.7 t ha^{-1}.

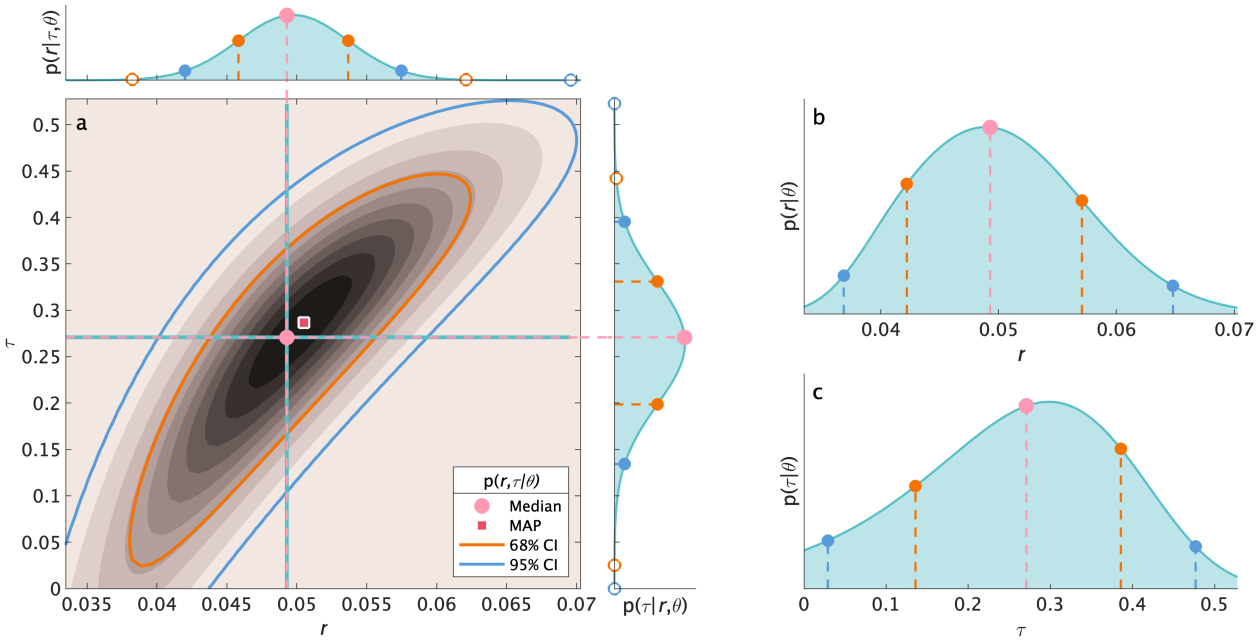

Figure 5: (a) The joint posterior distribution $p(r, \tau \mid \theta)$ for the rock application rate r and weathering extent τ. Here, $\theta = \{\Delta\text{Ti}, \Delta\text{Ca}, \Delta\text{Mg}\}_{\text{obs}}$ representing the vector of observed mean element changes. The highlighted contours denote 68% and 95% credible intervals. The mean and maximum a posteriori values are also highlighted. (b) The marginal posterior $p(r \mid \theta) = \int p(r, \tau \mid \theta)\, d\tau$, obtained by integrating the joint distribution over all values of τ. This integration propagates the full uncertainty in weathering extent into the reported credible intervals for r. Filled circles denote credible intervals derived from this marginal distribution; open circles show intervals from the conditional slice $p(r \mid \tau, \theta)$ at $\tau = \tilde{\tau}$ (panel a, top). The marginal intervals are wider because they account for uncertainty in τ rather than conditioning on a single value. (c) The marginal posterior $p(\tau \mid \theta) = \int p(r, \tau \mid \theta)\, dr$, obtained by integrating over all values of r. Credible intervals derived from this marginal (filled circles) properly represent our uncertainty in weathering extent given the data. The conditional slice $p(\tau \mid r, \theta)$ at $r = \tilde{r}$ (panel a, right; open circles) yields narrower intervals but implicitly assumes the rock fraction is known exactly.

4.2 Initial CDR estimation

The paired soil geochemistry (Ti, Ca, Mg) and basalt composition data presented in Section 3.3 are used to jointly constrain the rock fraction, r, and weathering extent, τ, through Bayesian inference (Section 3.4.1). We report initial CDR following Equation (4) with $L = 0$, representing gross CDR prior to geochemical and transport deductions.

Acknowledging that the initial CDR estimation presented here is an upper bound for net carbon removals, we find that the 620-acre (251 ha) study site could account for nearly 1,000 tons of CO_2 drawdown (1,025 tons CO_2 for $\hat{p}_{\text{MAP}}$). Note that the study site presented in this work accounts for only $\sim$ 29% of the total Kharif 2024 deployment (Table 1). If the weathering rate were to be similar across the immediate agroecological vicinity, the full studied deployment would have an integrated CO_2 drawdown potential of over 3,000 tons.

Table 4: Marginal posterior estimates, r, τ and implied CDR

	MAP	Median	68% CI	95% CI
r (rock fraction)	0.051	0.049	[0.042, 0.057]	[0.037, 0.065]
τ (weathering extent)	0.286	0.271	[0.136, 0.386]	[0.029, 0.477]
CDR (t CO_2 ac^{-1})	1.65	1.56	[0.78, 2.23]	[0.17, 2.75]
CDR (t CO_2 ha^{-1})	4.09	3.87	[1.94, 5.50]	[0.41, 6.80]
Deployment CDR (tons CO_2)	1025	969	[486, 1381]	[104, 1707]

CO_2 removal per acre is calculated as CDR $= E_{pot} \times \mathcal{A} \times \tau$, where τ is the weathering extent (see Section 3.4.1), $E_{pot} = 0.319$ tons CO_2/ton basalt is the drawdown potential computed from the sample-weighted basalt composition using Equation (3) and $\mathcal{A} = 18.1$ tons per acre (44.7 t ha^{-1}) is the application rate. The weathering study area was 620 acres (251 ha) across 2662 plots with 128 soil samples.

5 Discussion

5.1 Initial agronomic benefits of ERW in degraded soil

The measured yield increases observed following basalt application indicate that ERW can generate material agronomic benefits in smallholder rice systems. Our yield increases with ERW are consistent with those reported previously for ERW field trials with rice using wollastonite (12%) (Wang et al., 2024), while pot experiments with basalt have demonstrated enhanced elemental uptake and improved soil properties in paddy systems (Uchibayashi et al., 2025). More generally, these findings are consistent with a growing agronomic literature showing that finely ground silicate minerals can contribute to the restoration of degraded soils by improving soil chemical and physical properties in weathered tropical systems, particularly where baseline soil fertility and pH management are constrained (Silva et al., 2023; Pereira Seidel et al., 2021; Rodrigues et al., 2024; Rodrigues da Silva et al., 2024; Lozano-Baez and Camargo-Bernal, 2022; Almeida and Gomes, 2022; Wotchoko et al., 2021; Anda et al., 2015; Guo et al., 2023; Skov et al., 2024; Kelland et al., 2020; Beerling et al., 2024; Dietzen and Rosing, 2023; Haque et al., 2020; Edwards et al., 2017). In many smallholder landscapes, long-term nutrient mining, limited liming and declining organic matter have resulted in soil acidification, base cation depletion and reduced productive capacity, creating conditions under which silicate amendments may function as restorative inputs rather than marginal yield enhancers (Lal, 2015; IPCC, 2022).

Soil surveys in Chhattisgarh indicate that Alfisols and Inceptisols in the region are typically poor to medium in nitrogen and phosphorus, with potassium status varying from medium to adequate (Sharma et al., 2015). However, intensive rice cultivation has led to progressive potassium depletion across Indian rice systems, with the rice–wheat rotation in the Indo-Gangetic Plains removing up to 325 kg K ha^{-1} annually, often without adequate replacement (Singh et al., 2022; Timsina et al., 2021). Micronutrient deficiencies are widespread in local smallholder settings. Approximately 49% of Indian agricultural soils are deficient in zinc, with zinc being second only to nitrogen in importance for lowland rice production (Shukla et al., 2021; Sherpa et al., 2024). Silicon, though not classified as essential, is increasingly recognized as agronomically critical for sustainable rice production, with rice accumulating silicon at rates exceeding nitrogen uptake (Savant et al., 1997; Dobermann and Fairhurst, 2000).

The silicon contribution of basalt is particularly beneficial for rice systems (see Table 3 for approximate Si addition). Silicon strengthens plant cell walls (Ma and Yamaji, 2006; Jiang et al., 2025). Silicon-mediated strengthening of epidermal tissue enhances resistance to fungal pathogens including blast (*Magnaporthe oryzae*), brown spot (*Cochliobolus miyabeanus*), and sheath blight, diseases that impose substantial yield penalties in tropical rice systems (Datnoff and Rodrigues, 2005; Rodrigues et al., 2005). Under drought conditions, silicon improves water use efficiency and maintains photosynthetic function, effects that are increasingly relevant as monsoonal variability intensifies in central India (Chen et al., 2011; Cooke and Leishman, 2016). In highly weathered tropical soils where plant-available silicon is often depleted through desilication and continuous cropping, basalt application represents a means of restoring silicon supply to levels required for rice growth (Savant et al., 1997; McCarty et al., 2024).

The alkalinity contribution is quantified in Table 5. The combined release of Ca^{2+} and Mg^{2+} from weathering represents a calcium carbonate equivalence of 4.0 t ha^{-1}, or approximately 90 kg $CaCO_3$ per ton of basalt applied. This liming effect is particularly valuable in the moderately acidic Alfisols of the study region, where soil pH constraints can limit nutrient availability and root development (Sharma et al., 2015). Unlike conventional agricultural lime, which provides alkalinity without additional nutrients, basalt weathering couples *p*H amelioration with multi-element nutrient release, addressing the compound deficiencies characteristic of degraded smallholder soils. This effect, and the net potential CDR, are partially offset by uptake of major cations (Ca, Mg, K) by the crops. Bulk crop uptake is explored further in Figure 3 and SI C.2.

Table 5: Agricultural lime equivalence of basalt weathering

Parameter	Value
Basalt application rate	44.7 t ha^{-1}
Weathering extent, τ	0.27
Ca^{2+} released	21472.9 mol ha^{-1}
Mg^{2+} released	18622.3 mol ha^{-1}
$CaCO_3$ equivalence	4013.0 kg ha^{-1}
	4.01 t ha^{-1}
Per ton basalt applied	90 kg $CaCO_3$

Ag lime equivalence is calculated as $m_{CaCO_3} = (n_{Ca^{2+}} + n_{Mg^{2+}}) \times M_{CaCO_3}$, where n is moles released from basalt weathering and $M_{CaCO_3} = 100.1$ g mol^{-1}. This assumes equal acid-neutralizing capacity for each mole of divalent cation released.

A concern regarding large-scale ERW deployment is the potential for heavy metal contamination of agricultural soils and food crops (Dupla et al., 2023; Levy et al., 2024). Basalts may contain elevated concentrations of potentially toxic elements (PTEs) including nickel, chromium, and cadmium relative to typical agricultural soils, and models suggest that at high application rates (40 t ha^{-1} yr^{-1}) regulatory limits for certain elements could be exceeded within a decade of continuous application (Dupla et al., 2023). However, empirical studies of PTE accumulation in plant tissue following basalt amendment remain limited.

In this study, we found no evidence of PTE enrichment in rice biomass or soil following basalt application (Section 4.1). These findings are consistent with recent paddy rice studies: Uchibayashi et al. (2025) found no significant difference in arsenic, cadmium, chromium, copper, or nickel concentrations in rice grain across basalt application rates up to 100 t ha^{-1}, while Wang et al. (2024) observed decreased As and Cd concentrations in rice straw and grain following wollastonite treatment, attributed to enhanced silicon uptake. Our results also align with mesocosm studies of basalt application to potato crops, which found no significant increase in nickel concentrations in edible tubers despite elevated soil pore water nickel (Vienne et al., 2022), and with field trials in the US Corn Belt reporting no significant increase in trace metal content in maize or soybean grain following basalt amendment (Beerling et al., 2024). The modest sample sizes in this preliminary assessment ($n = 6$ for biomass, $n = 16$ for grain) limit statistical power of the study. Nevertheless, the larger soil data set, ($n = 128$) shows no significant evidence of PTE enrichment where basalt was applied (Table 8, SI A.2). The data provide an initial indication that single-season basalt application at the rates used in this study (44.7 t ha^{-1}) did not result in detectable PTE accumulation in harvested grain or straw, but longer-term monitoring across multiple cropping cycles will be essential to evaluate cumulative effects. Future work should systematically track soil PTE pools, plant uptake, and grain quality as ERW deployments mature, with particular attention to elements such as nickel and chromium that are enriched in mafic lithologies (Levy et al., 2024; Alloway, 2013).

5.2 Local and global welfare impacts of ERW

To contextualize the economic significance of the measured yield increases, baseline household income data were drawn from the Situation Assessment Survey, 77th Round (SAS-77) National Statistical Office (2021) covering the agricultural year July 2018 to June 2019. In Chhattisgarh, the primary state of deployment, the average

monthly income of an agricultural household was approximately ₹9,677 ($115) at 2018–19 prices, corresponding to an annual household income of around ₹116,000 ($1,381). As with most agricultural household surveys, these figures reflect total household income from a combination of crop production, wage labor, livestock and other activities. To ensure comparability with the 2024 season in which yield impacts were measured and valued, SAS 77 baseline incomes were uprated to 2024 prices using the MoSPI rural Consumer Price Index (CPI Rural, Base 2012=100; Ministry of Statistics and Programme Implementation, 2024). All subsequent percentage comparisons are therefore expressed in constant 2024 INR.

Applying the measured agronomic yield results from this study, the median estimated increase in gross revenue attributable to basalt application was approximately $303 per smallholder per year. Using an exchange rate of approximately 84 INR per USD, consistent with assumptions applied throughout this study, the increase in gross revenue corresponds to an additional ₹19,600–25,500 ($231–$303) annually in 2024 prices (Table 2). This revenue arises from additional rice sold through ordinary local markets at a Minimum Support Price and therefore not subject to price fluctuations from supply (Press Information Bureau, 2021). When expressed relative to the inflation-adjusted average agricultural household income for Chhattisgarh, this revenue increase represents approximately 15–25% of mean annual household earnings, relative to the inflation adjusted baseline income. The magnitude of these revenue uplifts is notable in the context of rural livelihoods in central India.

Empirical evidence consistently shows that rising smallholder incomes are systematically reinvested into farm productivity- enhancing assets, including mechanization, irrigation infrastructure, improved seed and fertilizer inputs an land improvement measures (Reardon et al., 2014; Duflo et al., 2011; Roodman, 2012), (Roodman, 2012; Dercon and Christiaensen, 2011; Banerjee et al., 2015; World Bank, 2018) In addition, income growth is consistently associated with improved educational outcomes (Duflo, 2001; Beegle et al., 2006; Dercon and Krishnan, 2000). ERW also generates global climate welfare gains: using a central estimate of the social cost of carbon of $185 per ton of CO_2 (Rennert et al., 2022), the MAP estimate of 1,025 tons of CO_2 removed within the weathering study area (620 acres; 251 ha) corresponds to approximately $190,000 in global welfare benefits, scaling to $443,000 when projected across acreage of the full deployment (2,188 acres; 886 ha, see Table 1). Simultaneously, yield-driven income gains generate direct local economic benefits of approximately $214,000 across participating households. These effects imply combined social and local welfare benefits of approximately $657,000 over the deployment period.

The monetization of the carbon removal attribute of ERW enables climate finance to underwrite the cost of soil restoration, thereby eliminating the need for farmer co-investment and accelerating adoption across liquidity constrained smallholder systems. Farmers, in turn, retain the full productivity and income gains generated by improved soil function, while society benefits from the long-term reduction in atmospheric carbon dioxide concentrations.

6 Conclusions

Modern food systems are complex and fragmented. Smallholder-dominated agricultural landscapes are subject to intersecting pressures of soil degradation, climate variability, volatile input markets and underinvestment. This study provides evidence that ERW can deliver agronomic benefits in smallholder rice systems. The observed the median increase in rice yields of 22.9%, results in revenue gains that are substantial relative to baseline household incomes in the region, increasing farm-level welfare and resilience.

Geochemical analysis of soil samples constrains the initial CDR potential at 1.6 (0.8–2.3) t CO_2 ac^{-1} (4.0 (2.1–5.7) t CO_2 ha^{-1}). The parallel climatic benefit of ERW, through durable carbon removal from the atmosphere, enables the monetization of climate value, potentially allowing the full costs of mineral sourcing, processing, application and monitoring to be financed without burden on the farmer or requiring public subsidy. The alignment of climate finance with agricultural productivity thus supports a pathway for commercial scale deployment of ERW across smallholder systems, a trajectory consistent with global projections indicating that the share of ERW-derived CDR from low- and lower-middle-income countries could rise from approximately 25% in 2040 to 60% by 2100, driven by accelerating adoption in climatically favorable regions such as the Indo-Gangetic Plain (Tu et al., 2026). These findings demonstrate the technical and economic feasibility of ERW as a coupled agronomic and climate intervention, capable of delivering durable atmospheric carbon removal alongside statistically significant yield and

income gains in smallholder-dominated agricultural systems in the Global South.

Acknowledgments

I.S.S. acknowledges support from Mati Carbon PBC. N.J.P. acknowledges support from Environmental Defense Fund. D.J.B. acknowledges support from the Leverhulme Trust. D.J.B. thanks Vicky Cobbold and David Martin of the Leverhulme Centre for Climate Change Mitigation for technical support.

Declaration of interests

J.S.J., T.M.D.M, J.B.S, R.D., A.D., D.P., R.M.R., N.K., F.A., M.T.T., L.Y.Y. and S.A. are at least partially employed by Mati Carbon PBC or Mati Carbon India Private Limited. M.T.T.'s contribution to this manuscript was not part of his University of Maryland nor NASA GSFC duties or responsibilities. D.J.B. has a minority equity stake in companies (Future Forest/Undo) and is an advisory board member of The Carbon Community, a UK carbon removal charity.

References

Ali, M. A., C. H. Lee, and P. J. Kim (2008). Effect of silicate fertilizer on reducing methane emission during rice cultivation. *Biology and Fertility of Soils 44*(4), 597–604.

Alloway, B. J. (2013). *Heavy Metals in Soils: Trace Metals and Metalloids in Soils and Their Bioavailability* (3rd ed.), Volume 22 of *Environmental Pollution*. Dordrecht: Springer.

Almeida, D. S. and N. Gomes (2022). Rock powder as a sustainable alternative for soil remineralization in tropical agriculture. *Journal of Cleaner Production 370*, 133432.

Amann, T. and J. Hartmann (2022). Carbon accounting for enhanced weathering. *Frontiers in Climate 4*, 849948.

Amann, T., J. Hartmann, E. Struyf, W. de Oliveira Garcia, E. K. Fischer, M. Konstantinos, and J. Krizik (2020). Enhanced weathering and related element fluxes—a cropland mesocosm approach. *Biogeosciences 17*, 103–119.

Anda, M., J. Shamshuddin, and C. I. Fauziah (2015). Improving chemical properties of a highly weathered soil using finely ground basalt rocks. *Catena 124*, 147–161.

Bach, L. T., S. J. Gill, R. E. M. Rickaby, S. Gore, and P. Renforth (2019). CO_2 removal with enhanced weathering and ocean alkalinity enhancement: Potential risks and co-benefits for marine pelagic ecosystems. *Frontiers in Climate 1*, 7.

Baek, S. H., Y. Kanzaki, J. M. Lora, N. Planavsky, C. T. Reinhard, and S. Zhang (2023). Impact of climate on the global capacity for enhanced rock weathering on croplands. *Earth's Future 11*(8), e2023EF003698.

Banerjee, A., E. Duflo, R. Glennerster, and C. Kinnan (2015). The miracle of microfinance? evidence from a randomized evaluation. *American Economic Journal: Applied Economics 7*(1), 22–53.

Beane, J. E., C. A. Turner, P. R. Hooper, K. V. Subbarao, and J. N. Walsh (1986). Stratigraphy, composition and form of the Deccan Basalts, Western Ghats, India. *Bulletin of Volcanology 48*(1), 61–83.

Beegle, K., R. H. Dehejia, and R. Gatti (2006). Child labor and agricultural shocks. *Journal of Development Economics 81*(1), 80–96.

Beerling, D. J., D. Z. Epihov, I. B. Kantola, M. D. Masters, T. Reershemius, N. J. Planavsky, C. T. Reinhard, J. S. Jordan, S. J. Thorne, J. Weber, M. Val Martin, R. P. Freckleton, S. E. Hartley, R. H. James, C. R. Pearce, E. H. DeLucia, and S. A. Banwart (2024). Enhanced weathering in the US Corn Belt delivers carbon removal with agronomic benefits. *Proceedings of the National Academy of Sciences 121*(9), e2319436121.

Beerling, D. J., E. P. Kantzas, M. R. Lomas, P. Wade, R. M. Eufrasio, P. Renforth, B. Sarkar, M. G. Andrews, R. H. James, C. R. Pearce, J.-F. Mercure, H. Pollitt, P. B. Holden, N. R. Edwards, M. Khanna, L. Koh, S. Quegan, N. F. Pidgeon, I. A. Janssens, J. Hansen, and S. A. Banwart (2020). Potential for large-scale CO_2 removal via enhanced rock weathering with croplands. *Nature 583*(7815), 242–248.

Beerling, D. J., J. R. Leake, S. P. Long, J. D. Scholes, J. Ton, P. N. Nelson, M. Bird, E. Kantzas, L. L. Taylor, B. Sarkar, M. Kelland, E. DeLucia, I. Kantola, C. Müller, G. Rau, and J. Hansen (2018). Farming with crops and rocks to address global climate, food and soil security. *Nature Plants 4*(3), 138–147.

Beerling, D. J., C. T. Reinhard, R. H. James, A. Khan, N. Pidgeon, and N. J. Planavsky (2025). Challenges and opportunities in scaling enhanced weathering for carbon dioxide removal. *Nature Reviews Earth & Environment 6*(10), 672–686.

Berger, J. O. (1985). *Statistical Decision Theory and Bayesian Analysis* (2nd ed.). New York: Springer-Verlag.

Boudinot, F. G., G. Dreyfus, C. Frederick, and Y. Powers (2023). Enhanced rock weathering in the Global South: Exploring potential for enhanced agricultural productivity and carbon dioxide drawdown. White paper, Precision Development and Institute for Governance & Sustainable Development.

Brimhall, G. H., O. A. Chadwick, C. J. Lewis, W. Compston, I. S. Williams, K. J. Danti, W. E. Dietrich, M. E. Power, D. Hendricks, and J. Bratt (1991). Deformational mass transport and invasive processes in soil evolution. *Science 255*(5045), 695–702.

Brimhall, G. H. and W. E. Dietrich (1987). Constitutive mass balance relations between chemical composition, volume, density, porosity, and strain in metasomatic hydrochemical systems: Results on weathering and pedogenesis. *Geochimica et Cosmochimica Acta 51*(3), 567–587.

Calabrese, S., B. Wild, M. B. Bertagni, I. C. Bourg, C. E. White, J. T. Abell, S. Silvestri, C. I. Steefel, and A. Porporato (2022). Nano- to global-scale uncertainties in terrestrial enhanced weathering. *Environmental Science & Technology 56*(22), 15261–15272.

Casella, G. and R. L. Berger (2002). *Statistical Inference* (2nd ed.). Pacific Grove, CA: Duxbury.

Castro, G. and C. A. C. Crusciol (2013). Effects of superficial liming and silicate application on soil fertility and crop yield under rotation. *Geoderma 195*, 234–242.

Central Ground Water Board, North Central Chhattisgarh Region (2023). Ground water yearbook 2022–2023 of chhattisgarh state. Technical report, Ministry of Jal Shakti, Government of India, Department of Water Resources, River Development and Ganga Rejuvenation, Raipur.

Chadwick, O. A., G. H. Brimhall, and D. M. Hendricks (1990). From a black to a gray box — a mass balance interpretation of pedogenesis. *Geomorphology 3*(3–4), 369–390.

Chadwick, O. A., L. A. Derry, P. M. Vitousek, B. J. Huebert, and L. O. Hedin (1999). Changing sources of nutrients during four million years of ecosystem development. *Nature 397*(6719), 491–497.

Chen, W., X. Yao, K. Cai, and J. Chen (2011). Silicon alleviates drought stress of rice plants by improving plant water status, photosynthesis and mineral nutrient absorption. *Biological Trace Element Research 142*(1), 67–76.

Cooke, J. and M. R. Leishman (2016). Consistent alleviation of abiotic stress with silicon addition: a meta-analysis. *Functional Ecology 30*(8), 1340–1357.

Cornu, S., Y. Lucas, E. Lebon, J.-P. Ambrosi, F. Luizão, J. Rouiller, M. Bonnay, and C. Neal (1999). Evidence of titanium mobility in soil profiles, Manaus, central Amazonia. *Geoderma 91*(3–4), 281–295.

Coskun, D., D. T. Britto, W. Q. Huynh, and H. J. Kronzucker (2016). The role of silicon in higher plants under salinity and drought stress. *Frontiers in Plant Science 7*, 1072.

Crusciol, C. A., A. C. Artigiani, O. Arf, A. C. Carmeis Filho, R. P. Soratto, A. S. Nascente, and R. C. Alvarez (2016). Soil fertility, plant nutrition, and grain yield of upland rice affected by surface application of lime, silicate, and phosphogypsum in a tropical no-till system. *Catena 137*, 87–99.

Datnoff, L. E. and F. A. Rodrigues (2005). The role of silicon in suppressing rice diseases. *APSnet Features*.

Dercon, S. and L. Christiaensen (2011). Consumption risk, technology adoption and poverty traps: Evidence from Ethiopia. *Journal of Development Economics 96*(2), 159–173.

Dercon, S. and P. Krishnan (2000). Vulnerability, seasonality and poverty in Ethiopia. *Journal of Development Studies 36*(6), 25–53.

Dietzen, C., R. Harrison, and S. Michelsen-Correa (2018). Effectiveness of enhanced mineral weathering as a carbon sequestration tool and alternative to agricultural lime: An incubation experiment. *International Journal of Greenhouse Gas Control 74*, 251–258.

Dietzen, C. and M. T. Rosing (2023). Quantification of CO_2 uptake by enhanced weathering of silicate minerals applied to acidic soils. *International Journal of Greenhouse Gas Control 125*, 103872.

Dobermann, A. and T. Fairhurst (2000). *Rice: Nutrient Disorders and Nutrient Management*. Singapore and Los Baños, Philippines: Potash and Phosphate Institute, Potash and Phosphate Institute of Canada, and International Rice Research Institute.

Duflo, E. (2001). Schooling and labor market consequences of school construction in Indonesia: Evidence from an unusual policy experiment. *American Economic Review 91*(4), 795–813.

Duflo, E., M. Kremer, and J. Robinson (2011). Nudging farmers to use fertilizer: Theory and experimental evidence from Kenya. *American Economic Review 101*(6), 2350–2390.

Duncan, R. A. and D. G. Pyle (1988). Rapid eruption of the Deccan flood basalts at the Cretaceous/Tertiary boundary. *Nature 333*(6176), 841–843.

Dupla, X., B. Kram, T. Thoenen, T. Gimmi, and S. V. Churakov (2023). Reversal of weathering: Secondary mineral formation during enhanced weathering in the laboratory. *Environmental Science & Technology 57*(43), 16311–16321.

Dupla, X., B. Möller, P. C. Baveye, and S. Grand (2023). Potential accumulation of toxic trace elements in soils during enhanced rock weathering. *European Journal of Soil Science 74*(1), e13343.

Edwards, D. P., F. Lim, R. H. James, C. R. Pearce, J. Scholes, R. P. Freckleton, and D. J. Beerling (2017). Climate change mitigation: potential benefits and pitfalls of enhanced rock weathering in tropical agriculture. *Biology Letters 13*(4), 20160715.

FAO (2011). Save and grow: A policymaker's guide to the sustainable intensification of smallholder crop production. Technical report, Food and Agriculture Organization of the United Nations, Rome.

FAO and ITPS (2015). Status of the world's soil resources (SWSR)—main report. *Food and Agriculture Organization of the United Nations and Intergovernmental Technical Panel on Soils*.

Feder, G., R. E. Just, and D. Zilberman (1985). Adoption of agricultural innovations in developing countries: A survey. *Economic Development and Cultural Change 33*(2), 255–298.

Fuss, S., W. F. Lamb, M. W. Callaghan, J. Hilaire, F. Creutzig, T. Amann, T. Beringer, W. de Oliveira Garcia, J. Hartmann, T. Khanna, G. Luderer, G. F. Nemet, J. Rogelj, P. Smith, J. L. V. Vicente, J. Wilcox, M. d. M. Zamora Dominguez, and J. C. Minx (2018). Negative emissions—part 2: Costs, potentials and side effects. *Environmental Research Letters 13*(6), 063002.

Gelman, A., J. B. Carlin, H. S. Stern, D. B. Dunson, A. Vehtari, and D. B. Rubin (2013). *Bayesian Data Analysis* (3rd ed.). Boca Raton, FL: CRC Press.

Gómez de la Peña, E., E. J. Rohling, J. F. Donges, J. Martín-Chivelet, R. L. Edwards, and H. Cheng (2020). Dynamics of carbonate precipitation in the Mediterranean region during the last 130,000 years. *Quaternary Science Reviews 228*, 106108.

Government of India (2025, August). Revision of usage charges for gunny bags. Ministry of Consumer Affairs, Food and Public Distribution, Press Release. Usage charges revised from ₹7.32 to ₹10.22 per bag, effective KMS 2025-26.

Guo, F., Y. Wang, H. Zhu, et al. (2023). Crop productivity and soil inorganic carbon change mediated by enhanced rock weathering in farmland: A comparative field analysis of multi-agroclimatic regions in central China. *Agricultural Systems 210*, 103691.

Hamilton, S. K., A. L. Kurzman, C. Arber, J. B. Paces, and G. P. Robertson (2007). Quantifying uncertainty in estimation of mineral weathering rates. *Earth and Planetary Science Letters 256*, 560–572.

Haque, F., R. M. Santos, and Y. W. Chiang (2020). Co-benefits of wollastonite weathering in agriculture: CO_2 sequestration and promoted plant growth. *ACS Omega 5*(3), 1425–1433.

Harrington, K. J., R. G. Hilton, and G. M. Henderson (2023). Implications of the riverine response to enhanced weathering for CO_2 removal in the UK. *Applied Geochemistry 152*, 105643. Carbonate precipitation reduces EW efficacy by 16% (10 t/ha) to 27% (50 t/ha) in UK catchments.

Hartmann, J., A. J. West, P. Renforth, P. Köhler, C. L. De La Rocha, D. A. Wolf-Gladrow, H. H. Dürr, and J. Scheffran (2013). Enhanced chemical weathering as a geoengineering strategy to reduce atmospheric carbon dioxide, supply nutrients, and mitigate ocean acidification. *Reviews of Geophysics 51*(2), 113–149.

IPCC (2007). Climate change 2007: Impacts, adaptation and vulnerability. In M. L. Parry, O. F. Canziani, J. P. Palutikof, P. J. van der Linden, and C. E. Hanson (Eds.), *Contribution of Working Group II to the Fourth Assessment Report of the Intergovernmental Panel on Climate Change*. Cambridge, UK: Cambridge University Press.

IPCC (2022). Climate change 2022: Mitigation of climate change. Technical report, Cambridge, UK and New York, NY, USA.

Itin-Shwartz, B. (2026). The effectiveness of 'in-market' and 'out-of-market' liberalization policies: Evidence from Indian produce markets. *International Journal of Industrial Organization 104*, 103234.

Jayne, T. S., S. Snapp, F. Place, and N. Sitko (2019). Sustainable agricultural intensification in an era of rural transformation in Africa. *Global Food Security 20*, 105–113.

Jaynes, E. T. (2003). *Probability Theory: The Logic of Science*. Cambridge: Cambridge University Press.

Jiang, H. et al. (2025). Silicon nutrition improves lodging resistance of rice under dry cultivation. *Plants 14*(3), 361.

Kantola, I. B., E. Blanc-Betes, M. D. Masters, E. Chang, A. Marklein, C. E. Moore, A. von Haden, C. J. Bernacchi, A. Wolf, D. Z. Epihov, D. J. Beerling, and E. H. DeLucia (2023). Improved net carbon budgets in the US Midwest through direct measured impacts of enhanced weathering. *Global Change Biology 29*(24), 7012–7028.

Kantola, I. B., M. D. Masters, D. J. Beerling, S. P. Long, and E. H. DeLucia (2017). Potential of global croplands and bioenergy crops for climate change mitigation through deployment for enhanced weathering. *Biology Letters 13*(4), 20160714.

Kelland, M. E., P. W. Wade, A. L. Lewis, L. L. Taylor, M. Mayall, R. H. James, J. A. Sheridan, M. G. Andrews, M. Sheridan, T. M. Sheridan, C. R. Pearce, D. Sheridan, D. Z. Epihov, A. Sheridan, R. Sheridan, and D. J. Beerling (2020). Increased yield and CO_2 sequestration potential with the C_4 cereal *Sorghum bicolor* cultivated in basaltic rock dust-amended agricultural soil. *Global Change Biology 26*(6), 3658–3676.

Kurtz, A. C., L. A. Derry, O. A. Chadwick, and M. J. Alfano (2000). Refractory element mobility in volcanic soils. *Geology 28*(8), 683–686.

Lal, R. (2015). Restoring soil quality to mitigate soil degradation. *Sustainability 7*(5), 5875–5895.

Lauerwald, R., G. G. Laruelle, J. Hartmann, P. Ciais, and P. A. G. Regnier (2015). Spatial patterns in CO_2 evasion from the global river network. *Global Biogeochemical Cycles 29*(5), 534–554.

Levy, C. R., M. Almaraz, D. J. Beerling, P. A. Raymond, C. T. Reinhard, T. J. Suhrhoff, and L. L. Taylor (2024). Enhanced rock weathering for carbon removal–monitoring and mitigating potential environmental impacts on agricultural land. *Environmental Science & Technology 58*(40), 17215–17226.

Liu, Z., W. Dreybrodt, and H. Wang (2011). A new direction in effective accounting for the atmospheric CO_2 budget: Considering the combined action of carbonate dissolution, the global water cycle and photosynthetic uptake of DIC by aquatic organisms. *Earth-Science Reviews 99*(3–4), 162–172.

Lowder, S. K., J. Skoet, and T. Raney (2016). The number, size, and distribution of farms, smallholder farms, and family farms worldwide. *World Development 87*, 16–29.

Lozano-Baez, S. E. and Ó. F. Camargo-Bernal (2022). Silicate rock powder as a potential source of nutrients for crops in tropical soils. *Agronomía Colombiana 40*(2), 208–218.

Ma, J. F. and N. Yamaji (2006). Silicon uptake and accumulation in higher plants. *Trends in Plant Science 11*(8), 392–397.

Mahoney, J. J., H. C. Sheth, D. Chandrasekharam, and Z. X. Peng (2000). Geochemistry of flood basalts of the Toranmal section, northern Deccan Traps, India: implications for regional Deccan stratigraphy. *Journal of Petrology 41*(7), 1099–1120.

McCarty, J. S., N. Sharma, R. Kumar, et al. (2024). Impact of silicon fertilization on crop growth, productivity and lodging resistance of rice: A review. *Plant Science Today 11*, 287.

Middelburg, J. J., K. Soetaert, and M. Hagens (2020). Ocean alkalinity, buffering and biogeochemical processes. *Reviews of Geophysics 58*(3), e2019RG000681.

Ministry of Statistics and Programme Implementation (2024). Consumer price index numbers on base 2012=100 for rural, urban and combined. National Statistical Office, Government of India. CPI (Rural) series, Base Year 2012=100.

Monger, H. C., R. A. Kraimer, S. Khresat, D. R. Cole, X. Wang, and J. Wang (2015). Sequestration of inorganic carbon in soil and groundwater. *Geology 43*(5), 375–378.

Mueller, N. D., J. S. Gerber, M. Johnston, D. K. Ray, N. Ramankutty, and J. A. Foley (2012). Closing yield gaps through nutrient and water management. *Nature 490*(7419), 254–257.

National Academies of Sciences, Engineering, and Medicine (2019). *Negative Emissions Technologies and Reliable Sequestration: A Research Agenda*. Washington, DC: The National Academies Press.

National Statistical Office (2021). Situation assessment of agricultural households and land and holdings of households in rural India, 2019. Nss report no. 587 (77/33.1/1), Ministry of Statistics and Programme Implementation, Government of India. SAS-77, covering agricultural year July 2018 to June 2019.

NITI Aayog (2021, June). Per metric ton kilometer cost of different modes of logistics in India. Government of India. Road transport: ₹3.6 per metric ton-km. Short-haul agricultural transport with loading/unloading typically 2–3× base rate. Available via Statista.

Pereira Seidel, G., M. Rodrigues, L. F. d. S. Junges, et al. (2021). Use of basalt rock powder as an alternative fertilizer culture of soybean. *Research, Society and Development 10*(6), e33710615599.

Perrin, A.-S., A. Probst, and J.-L. Probst (2008). Impact of nitrogenous fertilizers on carbonate dissolution in small agricultural catchments: Implications for weathering CO_2 uptake at regional and global scales. *Geochimica et Cosmochimica Acta 72*(13), 3105–3123. Demonstrated that nitric acid from fertilizer nitrification can offset 30% of CO_2 consumption by carbonic weathering.

Pogge von Strandmann, P. A. E., P. Renforth, A. J. West, M. J. Murphy, and M. Sheridan (2023). Field measurements of enhanced weathering. *Frontiers in Climate 5*, 1216224.

Press Information Bureau (2021). Procurement of rice on MSP. Government of India, Ministry of Consumer Affairs, Food and Public Distribution.

Probst, J.-L., J. Mortatti, and Y. Tardy (1994). Carbon river fluxes and weathering CO_2 consumption in the Congo and Amazon river basins. *Applied Geochemistry 9*(1), 1–13.

Raymond, P. A., J. Hartmann, R. Lauerwald, S. Sobek, C. McDonald, M. Hoover, D. Butman, R. Striegl, E. Mayorga, C. Humborg, P. Kortelainen, H. Dürr, M. Meybeck, P. Ciais, and P. Guth (2013). Global carbon dioxide emissions from inland waters. *Nature 503*, 355–359.

Reardon, T., C. P. Timmer, C. B. Barrett, and J. Berdegué (2014). The quiet revolution in agri-food systems: Transformation in the middle-income and developing countries. *Annual Review of Resource Economics 6*(1), 397–418.

Reershemius, T., M. E. Kelland, J. S. Jordan, I. R. Davis, R. D'Ascanio, B. Kalderon-Asael, D. Asael, T. J. Suhrhoff, D. Z. Epihov, D. J. Beerling, C. T. Reinhard, and N. J. Planavsky (2023). Initial validation of a soil-based mass-balance approach for empirical monitoring of enhanced rock weathering rates. *Environmental Science & Technology 57*(48), 19497–19507.

Renforth, P. (2012). The potential of enhanced weathering in the UK. *International Journal of Greenhouse Gas Control 10*, 229–243.

Renforth, P. (2019). The negative emission potential of alkaline materials. *Nature Communications 10*(1), 1401.

Renforth, P. and G. Henderson (2017). Assessing ocean alkalinity for carbon sequestration. *Reviews of Geophysics 55*(3), 636–674.

Rennert, K., F. Errickson, B. C. Prest, L. Rennels, R. G. Newell, W. Pizer, C. Kingdon, J. Wingenroth, R. Cooke, B. Parthum, D. Smith, K. Cromar, D. Diaz, F. C. Moore, U. K. Müller, R. J. Plevin, A. E. Raftery, H. Ševčíková, H. Sheets, J. H. Stock, T. Tan, M. Watson, T. E. Wong, and D. Anthoff (2022). Comprehensive evidence implies a higher social cost of CO_2. *Nature 610*(7933), 687–692.

Ricker-Gilbert, J. (2020). Inorganic fertiliser use among smallholder farmers in sub-Saharan Africa: implications for input subsidy policies. In *The Role of Smallholder Farms in Food and Nutrition Security*, pp. 81–98. Cham: Springer International Publishing.

Rodrigues, F. A., L. E. Datnoff, G. H. Korndörfer, K. W. Seebold, and M. C. Rush (2005). Silicon and rice disease management. *Fitopatologia Brasileira 30*(5), 457–469.

Rodrigues, M., C. Mozorovicz, G. S. Ziemmer, et al. (2024). Paraná basin basalt powder: A multinutrient soil amendment for enhancing soil chemistry and microbiology. *Journal of South American Earth Sciences 140*, 104929.

Rodrigues da Silva, L. J., A. d. S. Sandim, A. P. Rodrigues da Silva, A. C. F. Deus, J. A. Antonangelo, and L. T. Büll (2024). Evaluating the agronomic efficiency of alternative phosphorus sources applied in Brazilian tropical soils. *Scientific Reports 14*, 8526.

Roodman, D. (2012). *Due Diligence: An Impertinent Inquiry into Microfinance*. CGD Books.

Savant, N. K., L. E. Datnoff, and G. H. Snyder (1997). Depletion of plant-available silicon in soils: A possible cause of declining rice yields. *Communications in Soil Science and Plant Analysis 28*(13–14), 1245–1252.

Savant, N. K., G. H. Snyder, and L. E. Datnoff (1997). Silicon management and sustainable rice production. *Advances in Agronomy 58*, 151–199.

Semhi, K., P.-A. Suchet, N. Clauer, and J.-L. Probst (2000). Impact of nitrogen fertilizers on the natural weathering-erosion processes and fluvial transport in the Garonne basin. *Applied Geochemistry 15*(6), 865–878.

Sharma, G. K., V. N. Mishra, G. R. Maruti Sankar, S. K. Patil, L. K. Srivastava, D. S. Thakur, and C. Srinivasa Rao (2015). Soil-test-based optimum fertilizer doses for attaining yield targets of rice under midland Alfisols of eastern India. *Communications in Soil Science and Plant Analysis 46*(17), 2177–2190.

Sherpa, A. R., R. L. Sherpa, A. Kumar, et al. (2024). Soil zinc surveillance frameworks can inform human nutrition studies: opportunities in India. *Frontiers in Soil Science 4*, 1421652.

Shukla, A. K., S. K. Behera, A. Pakhre, and S. K. Chaudhari (2021). Deficiency of phyto-available sulphur, zinc, boron, iron, copper and manganese in soils of India. *Scientific Reports 11*, 19760.

Silva, A. M. d., M. L. Oliveira, et al. (2023). Low-grade silicate minerals as value-added natural potash fertilizer in deeply weathered tropical soil. *Geoderma 432*, 116403.

Singh, R., S. K. Chaudhari, D. K. Kundu, S. S. Sengar, and A. Kumar (2006). Soils of Chhattisgarh: Characteristics and water management options. Research Bulletin Publication No. 34, Water Technology Centre for Eastern Region, Indian Council of Agricultural Research, Bhubaneswar, Orissa, India. Bulk density value of 1.55 g/cc used for Chhattisgarh agricultural soils.

Singh, V. K., B. S. Dwivedi, K. N. Tiwari, K. Majumdar, M. Rani, S. K. Singh, and J. Timsina (2022). Ongoing soil potassium depletion under intensive cropping in India and probable mitigation strategies: A review. *Agronomy for Sustainable Development 42*, 4.

Sivia, D. S. and J. Skilling (2006). *Data Analysis: A Bayesian Tutorial* (2nd ed.). Oxford: Oxford University Press.

Skov, K., J. Wardman, M. Healey, et al. (2024). Initial results from enhanced weathering field trials on grazing land in New Zealand. *Applied Geochemistry 162*, 105927.

Smith, P., J. Adams, D. J. Beerling, T. Beringer, K. V. Calvin, S. Fuss, B. Griscom, N. Hagemann, C. Kammann, F. Kraxner, et al. (2019). Land-management options for greenhouse gas removal and their impacts on ecosystem services and the sustainable development goals. *Annual Review of Environment and Resources 44*, 255–286.

Snedecor, G. W. and W. G. Cochran (1989). *Statistical Methods* (8th ed.). Ames, IA: Iowa State University Press. Foundational text on blocking and paired designs; see p. 101 on matched-pair variance reduction.

Subbarao, K. V. (1988). Deccan flood basalts. In *Memoirs of the Geological Society of India*, Volume 10, pp. 1–393. Bangalore: Geological Society of India.

Suhrhoff, T. J. (2021). Phytoprevention of heavy metal contamination from terrestrial enhanced weathering: Can plants save the day? *Frontiers in Climate 3*, 820204.

Suhrhoff, T. J., T. Reershemius, J. S. Jordan, S. Li, S. Zhang, E. Milliken, B. Kalderon-Asael, Y. Ebert, R. Nyateka, J. T. Thompson, C. T. Reinhard, and N. J. Planavsky (2025). An updated framework and signal-to-noise analysis of soil mass balance approaches for quantifying enhanced weathering on managed lands. *Environmental Science & Technology 59*(49), 26440–26453.

Taylor, L. L., J. Quirk, R. M. S. Thorley, P. A. Kharecha, J. Hansen, A. Ridgwell, M. R. Lomas, S. A. Banwart, and D. J. Beerling (2016). Enhanced weathering strategies for stabilizing climate and averting ocean acidification. *Nature Climate Change 6*, 402–406.

Timsina, J., V. K. Singh, and K. Majumdar (2021). Timing potassium applications to synchronize with plant demand. In T. S. Murrell, R. L. Mikkelsen, G. Sulewski, R. Norton, and M. L. Thompson (Eds.), *Improving Potassium Recommendations for Agricultural Crops*, pp. 231–266. Cham: Springer.

Tittonell, P. and K. E. Giller (2013). When yield gaps are poverty traps: The paradigm of ecological intensification in African smallholder agriculture. *Field Crops Research 143*, 76–90.

Tu, Y., R. Rafols, Y. Xu, N. Butler, L. Ababneh, F. Tao, V. Ramanathan, B. Z. Houlton, and C. Liao (2026). Scaling up enhanced rock weathering for equitable climate change mitigation. *Communications Sustainability 1*, 32.

Uchibayashi, H., H. Maruyama, T. Watanabe, S. Hamamoto, Y. Toma, A. Nakao, K. Kurokawa, and T. Shinano (2025). Impact of basalt application on soil chemical properties and elemental uptake by paddy rice through enhanced rock weathering. *Soil Science and Plant Nutrition 71*(4), 484–495.

Van Soest, P. J. (2006). Rice straw, the role of silica and treatments to improve quality. *Animal Feed Science and Technology 130*(3-4), 137–171.

Vienne, A., S. Poblador, M. Portillo-Estrada, J. Hartmann, S. Ijiehon, P. Wade, and S. Vicca (2022). Enhanced weathering using basalt rock powder: Carbon sequestration, co-benefits and risks in a mesocosm study with *Solanum tuberosum*. *Frontiers in Climate 4*, 869456.

Wang, F., F. Zhu, D. Liu, A. Wang, R. Kang, Z. Quan, Y. Li, X. Chen, G. Li, E. A. Hobbie, and Y. Fang (2024). Wollastonite powder application increases rice yield and CO_2 sequestration in a paddy field in Northeast China. *Plant and Soil 502*, 589–603.

Wild, B., D. Daval, E. Beaulieu, M.-C. Pierret, D. Viville, and G. Imfeld (2024). Silicate weathering in soils and watersheds. *Elements 20*(1), 31–37.

World Bank (2007). World development report 2008: Agriculture for development. Technical report, World Bank, Washington, DC.

World Bank (2018). Poverty and shared prosperity 2018: Piecing together the poverty puzzle. Technical report, World Bank, Washington, DC.

Wotchoko, P., J. F. Tene Djoukam, A. P. Kouske, et al. (2021). Agronomic potential of volcanic rocks from the Mount Bambouto, Cameroon Western Highlands. *Heliyon 7*(5), e07039.

Xu, T., H. Li, S. Vicca, D. S. Goll, D. J. Beerling, Q. Chen, B. Bi, Z. Yang, X. Wang, and Z. Yuan (2025). Enhanced rock weathering promotes soil organic carbon accumulation: A global meta-analysis based on experimental evidence. *Global Change Biology 31*(9), e70483.

Zamanian, K., K. Pustovoytov, and Y. Kuzyakov (2016). Pedogenic carbonates: Forms and formation processes. *Earth-Science Reviews 157*, 1–17.

Zar, J. H. (2010). *Biostatistical Analysis* (5th ed.). Upper Saddle River, NJ: Prentice-Hall. Chapter 9: Paired-Sample Hypotheses.

Zeebe, R. E. and D. Wolf-Gladrow (2001). *CO_2 in Seawater: Equilibrium, Kinetics, Isotopes* (1st ed.), Volume 65 of *Elsevier Oceanography Series*. Amsterdam: Elsevier.

Zhang, S., N. J. Planavsky, J. Katchinoff, P. A. Raymond, Y. Kanzaki, T. Reershemius, and C. T. Reinhard (2022). River chemistry constraints on the carbon capture potential of surficial enhanced rock weathering. *Limnology and Oceanography 67*(S2), S148–S157. Estimated $\leq$5% loss from riverine degassing and precipitation at 10% weathering product export.

A Supporting data explainer

A.1 Comparison of direct measurement and farmer surveys for rice yield

We interpret these results as evidence of a real, positive yield effect from basalt, but with different confidence levels depending on the measurement approach (Table 6). The directly measured data provide the cleaner estimate because the measurement scale is consistent across farms and does not mechanically amplify error at low baseline yields (Figure 6a). By contrast, the farmer survey series is directionally consistent but noisier and systematically biased by heteroscedasticity: farmers report harvest in whole quintals, so the same absolute rounding error becomes a much larger percentage error when baseline yields are small (Figure 6c). When yield response is expressed as a ratio relative to baseline yield, this rounding effect can inflate apparent gains for small harvests and widen the spread of responses, even if the underlying agronomic impact is similar. The distribution of plot areas across the deployment illustrates the smallholder agricultural setting typical of the region, with a median plot size of just 0.20 acres (Figure 6b). The implication is that the survey data are still useful for triangulating impact and for understanding adoption and real world variation across a large sample, but they should not be treated as the primary basis for precise effect sizing. Direct measurement should be used for calibration and claims and use large scale survey findings for coverage, perception, contextual interpretation and to inform targeting rather than headline magnitude.

Table 6: Unitless yield response, ΔPW, from basalt application. $\Delta PW = (Y_{\text{basalt}} - Y_{\text{control}})/Y_{\text{control}}$. Precision-weighted estimates correct for heteroscedasticity in farmer-reported data (larger baseline yields have smaller relative measurement error).

	Measured (3×1 m^2 patches)	**Survey** (farmer-reported)
n	44	594
Unweighted		
Mean ΔPW	27.5%	16.9%
95% CI	23.0–32.0%	15.4–18.5%
Median (IQR)	22.9% (17.5–30.9)	12.5% (7.7–20.8)
p-value	$<$0.001	$<$0.001
Precision-weighted[†]		
Mean ΔPW	24.8%	13.8%
95% CI	21.0–28.6%	12.6–14.9%
n_{eff}	40	549
p-value	$<$0.001	$<$0.001
Positive response ($\Delta PW > 0$)	100.0%	88.0%

[†]Farmers report whole quintals, so relative measurement precision scales with baseline yield. As an illustrative example, a 5 Q harvest has $\sim$10% resolution while a 50 Q harvest has $\sim$1% resolution. For $\Delta PW = \Delta Y / Y_{\text{control}}$ with measurement uncertainty σ:

$$\text{Var}(\Delta PW) \approx \frac{\sigma^2}{Y_{\text{control}}^2}$$

If $\sigma \propto \sqrt{Y}$ (Poisson-like natural variability), then $\text{Var}(\Delta PW) \propto 1/Y_{\text{control}}$. Inverse-variance weighting gives $w_i \propto Y_{\text{control},i}$, downweighting noisier observations from smaller harvests. Effective sample size $n_{\text{eff}} = (\sum w_i)^2 / \sum w_i^2$.

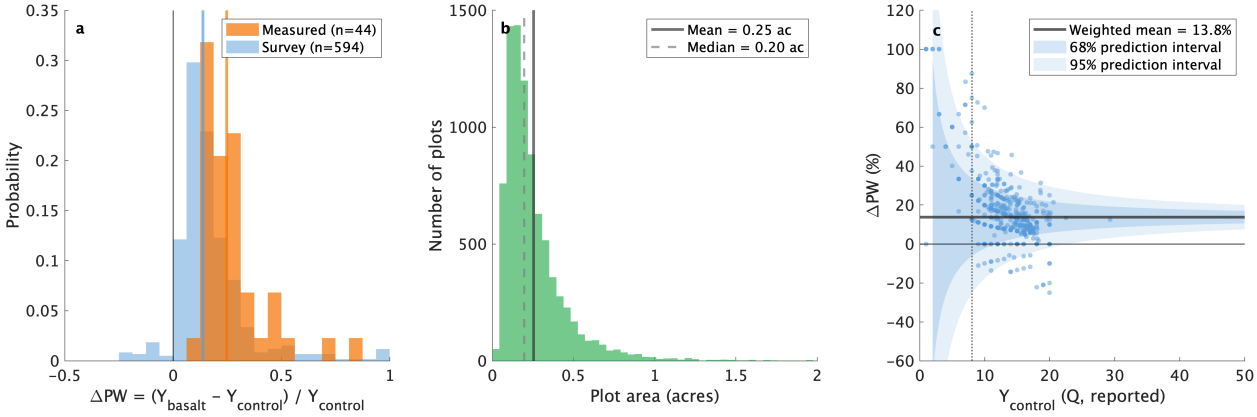

Figure 6: Unitless yield response (ΔPW) from basalt application according to directly measured fields and surveys. (a) Distribution of $\Delta\text{PW} = (Y_{\text{basalt}} - Y_{\text{control}})/Y_{\text{control}}$ for measured ($n = 44$, $3{\times}1\text{m}^2$ patch samples) and farmer-reported survey ($n = 594$) data. Vertical lines indicate precision-weighted means (24.8% and 13.8%, respectively). Both methods detect a statistically significant positive yield response ($p < 0.001$). (b) Distribution of plot areas across the deployment ($n = 8600$ plots, median $= 0.20$ acres; 0.08 ha), providing context for the smallholder agricultural setting typical of the region. (c) Survey ΔPW versus baseline yield, Y_{control}, in smallholder fields of unconstrained size. It illustrates that the survey data has strong heteroscedasticity—the statistical property where measurement uncertainty varies systematically across observations. Here, farmers reporting smaller baseline harvests show greater variability in their estimated ΔPW because the same absolute measurement error (in this case rounding to whole quintals) represents a larger relative error when divided by a small denominator. Shaded regions show 68% and 95% prediction intervals from a model where $\text{SD}(\Delta\text{PW}) = \sigma/Y_{\text{control}}$ ($\sigma = 1.61$). The dotted vertical line marks $Y_{\text{control}} = 8$ Q, above which the prediction interval narrows to $\pm$20%. This "reliable" subpopulation ($n = 543$, 91% of survey respondents) exhibits substantially reduced variance (SD $=$ 11.2% vs. 19.4%) and yields a mean ΔPW of 13.3% (95% CI: 12.4–14.3%), with 87% of farmers reporting positive yield gains. It is worth noting here that the surveys are intrinsically anecdotal. For such low precision information gathering, the heteroscedastic tendencies of this data set could be underestimated.

A.2 Soil data supplement

A.2.1 Soil sampling method

Fields for sampling are selected to optimize spatial representation; sampled fields are not directly adjacent. At Mati deployment sites, a hard claypan is typically present at shallow depth, such that traditional augers and soil corers are often unable to effectively collect soil from rice paddies. Mati therefore employs a trench-based sampling approach using spades or hoes to create a shallow ($\sim$15 cm) trench. While this method differs from traditional soil-coring protocols, it is adapted to the unique field conditions encountered in these systems. It is described below:

1. Remove the topsoil layer and surface debris.
2. Using a spade or hoe, create a wedge-shaped cut to a depth of $\sim$15 cm, confirmed in the field with a measuring stick.
3. Make a second angular cut into the soil wedge to sample the sidewalls, ensuring equal volumes from each soil horizon to the target depth.
4. Disaggregate the sample and spread it onto a clean plastic sheet in the field.
5. Homogenize the unconsolidated soil manually using the spade or hoe and by hand with clean nitrile gloves.
6. Divide the homogenized sample into four quadrants of equal volume; randomly select two quadrants as the final sample.
7. Transfer approximately 250 g of soil into pre-labeled sample bags.
8. Backfill each trench to restore the field surface.

A.2.2 Soil compositional data

Soil was digested and analyzed at an ISO/IEC 17025:2017 accredited private laboratory in Bengaluru, India. The soil is digested using 4-acid, 2-acid and peroxide fusion and measured for 63 elements. Data is reported depending on the elemental abundance and refractory nature of the material (i.e, Ti is reported from the peroxide fusion digest). All samples are ran with the certified reference material OREAS 231 and results are reported as the recovery for each element in ppm.

Table 7: Recovery percentages for Ca, Mg and Ti from OREAS 231 certified reference material across soil analytical runs/batches

Batch	Ca Recovery (%)	Mg Recovery (%)	Ti Recovery (%)
G2511	100.22	100.80	99.87
G2514	99.94	101.35	100.34
G2524	99.88	101.64	100.29
Recovery % = (Measured Value / Certified Value) $\times$ 100			
Certified values: Ca = 74,700 ppm; Mg = 39,000 ppm; Ti = 6,170 ppm			

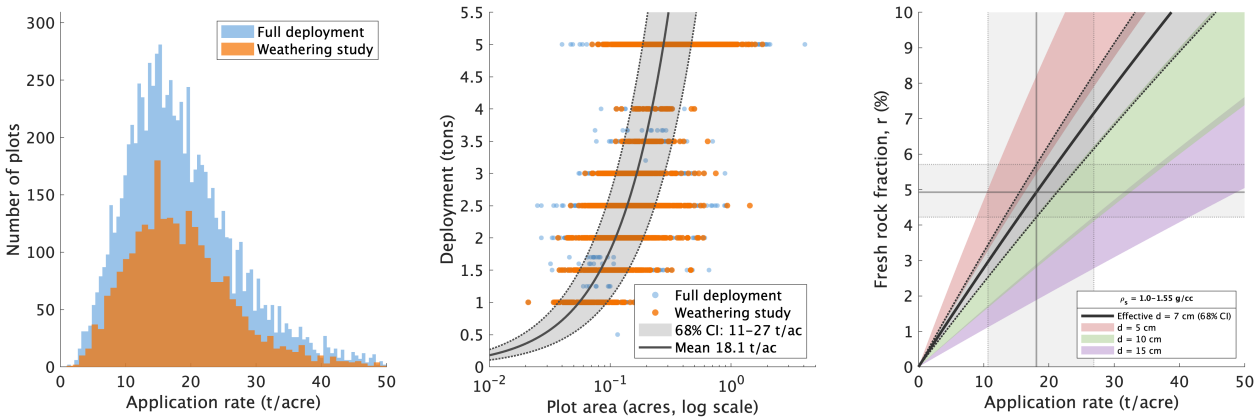

Figure 7: The relationships between application rate and sampling depth are explored. Alfisols in Chhattisgarh have a typical density of $\sim \rho = 1.55$ g cc^{-1} (Singh et al., 2006). Based on the range in actual recorded application rate across the deployment and $\hat{p}_{\text{MAP}}$, a mixing bias towards shallower sampling is observed (6–8 cm). This demonstates the importance of resolving an effective immobile element signal for basalt application while calculating the extent of weathering with this particular methodology.

Table 8: Soil concentrations of potentially toxic elements before (Pre-sample) and after (EOY) basalt application. Values are median with 68% interval (16th–84th percentile) in mg kg^{-1}.

Element	Pre-sample	EOY
Co	8.3 [6.3–12.1]	4.4 [2.0–10.8]
Cr	221.5 [204.0–268.4]	251.5 [210.3–294.0]
Cu	18.0 [13.3–25.0]	22.0 [17.0–35.0]
Nb	8.8 [7.2–10.9]	8.6 [4.9–10.8]
Ni	20.5 [15.0–28.7]	24.5 [17.3–34.0]
Pb	20.0 [16.0–27.0]	24.0 [19.3–29.0]
Th	2.0 [1.5–2.9]	4.8 [2.0–11.8]
U	2.2 [1.9–2.7]	1.9 [1.4–2.6]
V	54.5 [41.0–71.0]	63.5 [48.0–86.7]
Zn	30.0 [24.3–40.0]	34.0 [25.0–51.7]

A.3 Basalt data supplement

A.3.1 Basalt sampling method

In this study, basalt feedstocks were sourced as waste fines from rock crushers or surface quarries producing aggregate material for the construction of roads and buildings. The source of the material is various units in the Deccan Traps flood basalt deposits. Basalt waste fine dust is generally kept in piles at the rock crushers/quarries where they are produced. On average, a sampling frequency of 1 feedstock analysis per 875 tons of feedstock was used, where the minimum was 1 per 3,815.

A.4 Basalt sampling protocol

Basalt feedstock samples were collected from dust piles located at Mati Carbon partnered source quarries. At each crusher location, sourced material is stored in a single pile following sorting and conveying for different use cases (e.g., ∼10 mm aggregate for road construction). The sampling procedure is as follows:

1. Pool 8–10 sub-samples from a given dust pile to comprise a full basalt sample.
2. Collect 250–500 g of material directly from the vicinity of the crushers.
3. Pass pooled samples through a 2 mm sieve to remove large particles. Mati Carbon provides sieves to crushers selected for deployment.

A.4.1 Basalt compositional data

Basalt was digested and analyzed at an ISO/IEC 17025:2017 accredited private laboratory in Bangalore, India. Separate splits of soil are digested using 4-acid, 2-acid and peroxide fusion and measured for 63 elements. Data is reported depending on the elemental abundance and refractory nature of the material (i.e, Ti is reported from the peroxide fusion digest). All samples are ran with the certified reference material OREAS 231 and results are reported as the recovery for each element in ppm.

Table 9: Recovery percentages for Ca, Mg and Ti from OREAS 231 certified reference material for basalt analytical runs/batches

Batch	Ca Recovery (%)	Mg Recovery (%)	Ti Recovery (%)
G2513	100.19	101.67	99.89
G3691	100.06	102.88	99.97
Recovery % = (Measured Value / Certified Value) × 100			
Certified values: Ca = 74,700 ppm; Mg = 39,000 ppm; Ti = 6,170 ppm			

Basalt from eight individual quarries was applied at the Kharif 2024 study site examined in this study. To account for the heterogeneity in basalt sourcing, we compute a deployment-weighted average basalt composition for the study area to estimate the CDR potential of the feedstock. In addition, we calculate the sample-weighted average basalt needed for the Bayesian analysis associated with the 128 sample pairs used to calculate the extent of feedstock weathering, τ. The effective basalt composition is given

$$X_b = \frac{\sum_j w_j \cdot X_{b,j}}{\sum_j w_j}, \tag{12}$$

where w_j is the total mass of source j deployed (in tons) and $X_{b,j}$ is the mean composition of source j from laboratory analyses. This weighting reflects a composite basalt endmember applied to the deployed plots in the study area (see Table 10). Here we caution that X_b is a weighted mass-fraction and should not be confused for the stand-in notation for a mobile cations as in Section 3.4.1 or SI B.

Table 10: Basalt oxide composition and molar cation contributions

Oxide	Element (ppm)	wt%	M (g/mol)	Steinour coef.	mol/100g
Deployment-weighted:					
CaO	Ca (71000)	9.93	56.08	+1	0.17716
MgO	Mg (37485)	6.22	40.30	+1	0.15423
Na_2O	Na (14466)	1.950	61.98	+1	0.03146
K_2O	K (1579)	0.190	94.20	+1	0.00202
Corrections (cations bound to sulfate and phosphate):					
SO_3	S (275)	0.069	80.06	−1	-0.00086
P_2O_5	P (831)	0.190	141.94	−1	-0.00134
Net alkalinity potential of basalt feedstock (mol/100g):					0.363
E_{pot} (tons CO_2/ton basalt):					0.319
Sample-weighted:					
CaO	Ca (70951)	9.93	56.08	+1	0.17703
MgO	Mg (37373)	6.20	40.30	+1	0.15377
Na_2O	Na (14523)	1.958	61.98	+1	0.03159
K_2O	K (1667)	0.201	94.20	+1	0.00213
Corrections (cations bound to sulfate and phosphate):					
SO_3	S (278)	0.069	80.06	−1	-0.00087
P_2O_5	P (834)	0.191	141.94	−1	-0.00135
Net alkalinity potential of basalt feedstock (mol/100g):					0.362
E_{pot} (tons CO_2/ton basalt):					0.319

Deployment-weighted composition weights each basalt source by tons deployed (11210 tons total). Sample-weighted composition weights each source by number of soil samples collected (128 samples). Steinour coefficients represent moles of CO_2 sequestered per mole of oxide dissolved.

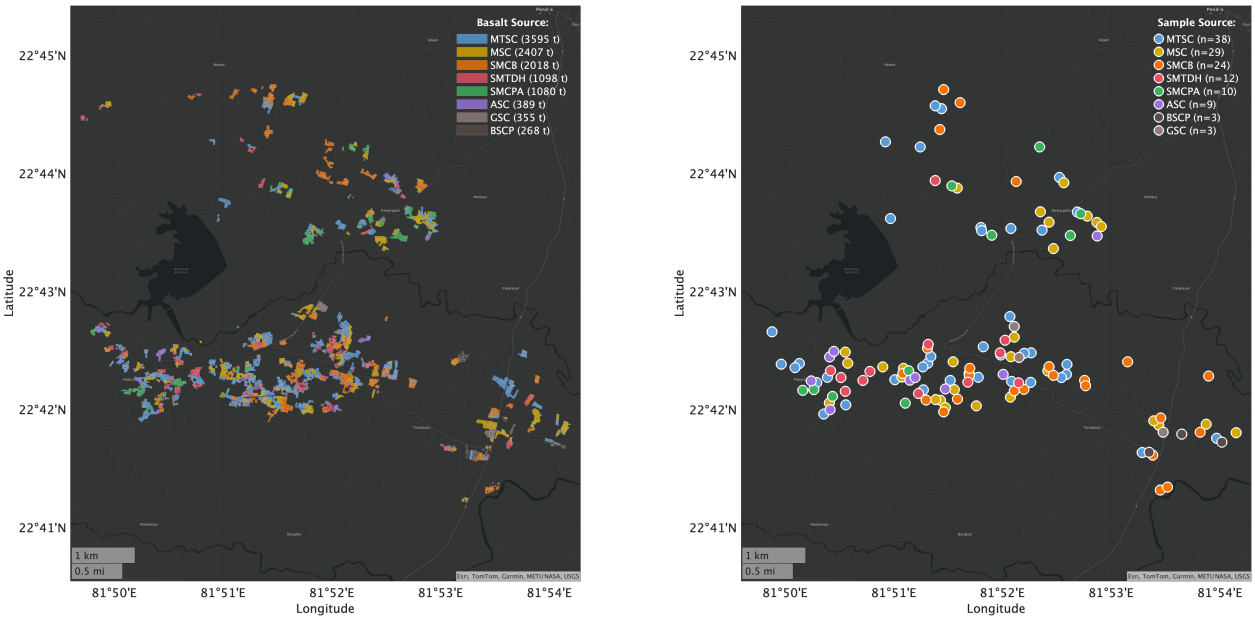

Figure 8: Maps showing the Weathering study area: sub-deployment region for Kharif 2024. Here, the various sources of basalt that were deployed in this sub-deployment (red box in Figure 1 b) are shown as polygons and color coded. The sample basalt sources associated with individual fields are shown as color coded points.

B Bayesian framework

B.1 Geochemical mass balance context

The use of immobile elements to track mass changes during weathering has a long history in geochemistry. The foundational framework was developed by Brimhall and Dietrich (1987) and formalized by Brimhall et al. (1991), who introduced the mass transfer coefficient $\tau_{j,i}$ (distinct from our τ) to quantify elemental gains and losses relative to an immobile reference element during pedogenesis. In their formulation,

$$\tau_{j,i} = \frac{C_{j,w}}{C_{j,p}} \frac{C_{i,p}}{C_{i,w}} - 1 \tag{13}$$

where C denotes concentration, subscripts j and i refer to the mobile and immobile elements and w and p denote weathered and parent material. This approach was extended by Chadwick et al. (1990) and has become somewhat standard in soil geochemistry.

The application of mass balance approaches to enhanced rock weathering (ERW) requires adaptation of this classical framework. Rather than tracking weathering of a single parent material into soil, ERW systems involve amendment of an existing soil with a secondary mineral phase (the feedstock), creating a three-endmember mixing problem. Reershemius et al. (2023) provided the initial validation of a soil-based mass balance approach for ERW, demonstrating that changes in immobile element concentrations (Ti, Zr, Nb) could be used to constrain feedstock addition rates, while mobile element depletion (Ca, Mg, Na, K) relative to immobile enrichment could quantify weathering extent. Suhrhoff et al. (2025) subsequently formalized this framework and conducted a signal-to-noise analysis, identifying the conditions under which soil mass balance approaches yield reliable weathering estimates. They emphasize that the approach is most robust when

1. feedstock and soil endmembers are compositionally distinct,
2. application rates are sufficient to generate detectable signals above analytical and sampling uncertainty,
3. immobile elements are truly conservative in the system of interest.

The formulation presented here follows this general approach but differs in parameterization. We define τ as the fractional extent of feedstock weathering rather than directly as a mass transfer coefficient, allowing it to be interpreted as the proportion of applied feedstock that has undergone cation release at a snapshot in time.

B.2 Immobile element assumption

The selection of titanium as an immobile reference element follows established practice in weathering studies (Brimhall et al., 1991; Kurtz et al., 2000; Chadwick et al., 1999). Titanium is considered relatively immobile during chemical weathering due to its low solubility under typical soil pH conditions and its residence in refractory mineral phases such as ilmenite, rutile and titanite. However, Ti mobility can occur under certain conditions, including extreme acidity, high organic ligand concentrations, or in systems with significant colloidal transport (Cornu et al., 1999; Kurtz et al., 2000).

For ERW applications, Reershemius et al. (2023); Suhrhoff et al. (2025) evaluated multiple candidate immobile elements (Ti, Zr, Nb, Hf, Th) and found that Ti generally provides reliable constraints when feedstock Ti concentrations substantially exceed those of the amended soil. In our system, basalt feedstock contains 2.6% TiO_2 (mean) compared to 0.46% in background soils (mean).

B.3 Forward model derivation

Consider a unit mass of post-deployment soil composed of mass fractions f_s, f_b and f_w of soil, unweathered basalt and weathered residue respectively, where $f_s + f_b + f_w = 1$. For any element E, the post-deployment concentration is given by the mass-weighted sum of endmember contributions:

$$E^{\text{post}} = f_s E_s + f_b E_b + f_w E_w \tag{14}$$

where E_s, E_b and E_w are the elemental concentrations in soil, unweathered basalt and weathered residue respectively.

We parameterize this system using the initial rock application rate r and the weathering extent τ:

$$r = f_b + f_w \tag{15}$$

$$\tau = \frac{f_w}{f_b + f_w} = \frac{f_w}{r} \tag{16}$$

These definitions yield $f_b = r(1-\tau)$, $f_w = r\tau$ and $f_s = 1 - r$.

For an immobile element I, weathering concentrates the element in the residue. However, when mass loss is small or the immobile element signal is dominated by the soil-basalt contrast, we can approximate $I_w \approx I_b$, giving:

$$\Delta I = I^{\text{post}} - I_s = r(I_b - I_s) \tag{17}$$

This result is independent of τ because immobile elements are conserved regardless of weathering extent.

For mobile elements X, we assume the weathered residue is completely depleted in mobile cations ($X_w = 0$). The change in mobile element concentration is then:

$$\Delta X = r\left[(1-\tau)X_b - X_s\right] \tag{18}$$

which can be rewritten as:

$$\Delta X = r(1-\tau)(X_b - X_s) - r\tau X_s \tag{19}$$

The first term represents addition of unweathered basalt cations reduced by weathering; the second term captures dilution of soil cations by weathered residue. When $X_b \gg X_s$, the dilution term is negligible and we recover the simplified form:

$$\Delta X \approx r(1-\tau)(X_b - X_s) \tag{20}$$

This simplified formulation is consistent with the TiCAT (Titanium-Cation) approach introduced by Reershemius et al. (2023). Section B.6 presents a sensitivity analysis comparing this model against more complex alternatives.

B.4 Bulk density independence

A practical advantage of this formulation is that it does not require measurements of soil bulk density. The rock mass fraction r can be determined directly from tracer enrichment:

$$r = \frac{I_{\text{mix}} - I_s}{I_b - I_s} \tag{21}$$

This ratio depends only on endmember compositions and the mass fraction, not on absolute sampled mass or bulk density. Many mass balance approaches require converting concentrations to areal masses via $M = C \cdot \rho_b \cdot h$, where ρ_b is bulk density and h is sampling depth (e.g. Suhrhoff et al. (2025)). Our concentration-ratio approach circumvents this by working entirely with ratios that are independent of sampled mass. This approach reduces measurement burden, avoids assumptions about constant volume between sampling events and maintains compatibility with standard agronomic soil testing.

B.5 Bayesian inference

We adopt a Bayesian approach to parameter estimation (Gelman et al., 2013; Sivia and Skilling, 2006). The posterior distribution $p(r, \tau \mid \theta)$ represents our state of knowledge about the parameters given observations θ.

B.5.1 Likelihood

We assume measurement errors for each element are independent, yielding a factorized likelihood:

$$\mathcal{L}(\theta \mid r, \tau) = \prod_{\mathcal{E}} \mathcal{L}_{\mathcal{E}} \tag{22}$$

For each element, we model the sampling distribution of the observed mean change as Gaussian, justified by the Central Limit Theorem (Casella and Berger, 2002):

$$\mathcal{L}_{\mathcal{E}} = \frac{1}{\sqrt{2\pi}\sigma_{\mathcal{E}}} \exp\left(-\frac{(\Delta\mathcal{E}_{\text{obs}} - \Delta\mathcal{E}_{\text{pred}})^2}{2\sigma_{\mathcal{E}}^2}\right) \tag{23}$$

where $\sigma_{\mathcal{E}} = s_{\mathcal{E}}/\sqrt{n}$ is the standard error of the mean.

B.5.2 Priors

We employ uninformed priors reflecting maximum ignorance within physical bounds (Jaynes, 2003):

$$p(r) \propto 1 \quad \text{for } r \in [0, r_{\text{max}}] \tag{24a}$$

$$p(\tau) \propto 1 \quad \text{for } \tau \in [0, 1]. \tag{24b}$$

B.5.3 Posterior computation

The posterior is given by Bayes' theorem,

$$p(r, \tau \mid \theta) = \frac{\mathcal{L}(\theta \mid r, \tau) \cdot p(r) \cdot p(\tau)}{\int\int \mathcal{L}(\theta \mid r', \tau') \cdot p(r') \cdot p(\tau')\, dr'\, d\tau'}. \tag{25}$$

Here, we compute the posterior via grid-based evaluation rather than using a full Markov-Chain Monte Carlo method (MCMC). For low-dimensional problems (here, $d = 2$), grid evaluations are easier. We have deterministic results and can blithely ignore issues pertaining to chain convergence or burn-in diagnostics and we have simple, direct access to the full joint posterior surface (Gelman et al., 2013). The primary limitation is computational cost scaling, which is negligible for two parameters. Were we to extend this framework to additional parameters, MCMC would become essential.

B.6 Forward model sensitivity analysis

We compare three forward model formulations of increasing complexity to validate the simplified model used in our primary analysis. The simplified model (Equations 20) assumes $X_b \gg X_s$ for mobile cations and $I_w \approx I_b$ for immobile elements. The dilution-corrected model (Equation 18) retains the full mass balance without the $X_b \gg X_s$ assumption, adding a dilution term $-r\tau X_s$. The dilution + enrichment-corrected model accounts for concentration of immobile elements in weathered residue via $I_w = I_b/(1-\lambda)$, where $\lambda = \tau f_{\text{sol}}$ is fractional mass loss. For the data presented in this work, $\text{Ca}_b/\text{Ca}_s = 17.9$ and $\text{Mg}_b/\text{Mg}_s = 14.6$, supporting the $X_b \gg X_s$ approximation. The dissolvable fraction (assuming aluminosilicate clays form in-situ as weathering products) $f_{\text{sol}} \sim 0.18$ implies only 5% mass loss at $\tau = 0.27$, making the immobile enrichment correction second-order (Table 11). In the current state of data collection where natural sample variance due to geochemical heterogeneity dominates, the simplest model is appropriate and sufficient. We adopt the simplified model because corrections to the forward model compared to the dilution-corrected and dilution + enrichment-corrected models are small relative to overall posterior and underlying measurement uncertainty.

Table 11: Calculation of soluble mass fraction f_{sol} from basalt composition.

Element	Approx. conc. (ppm)	M_E	M_{ox}	Stoich.	wt% oxide
Ca	70000	40.08	56.08	1	9.79
Mg	37000	24.31	40.30	1	6.13
Na	14500	22.99	61.98	2	1.95
K	2000	39.10	94.20	2	0.24
Total soluble oxides					18.11
f_{sol} (fraction)					0.181

M_E = element molar mass (g/mol); M_{ox} = oxide molar mass. Oxide wt% calculated as: wt% $= C \times 10^{-4} \times (M_{ox}/(n \times M_E))$, where C is concentration in ppm and n is stoichiometry. S and P are neglected here as they are roughly an order of magnitude less abundant than K in the feedstock.

Table 12: Posterior estimates across forward model formulations.

Parameter	Simplified	Dilution-corrected	Dilution + enrichment-corrected
r (median)	0.0493	0.0493	0.0484
r (68% CI)	[0.042, 0.057]	[0.042, 0.057]	[0.042, 0.056]
τ (median)	0.271	0.254	0.242
τ (68% CI)	[0.14, 0.39]	[0.13, 0.36]	[0.12, 0.34]
CDR (t CO_2/ha)	1.564	1.467	1.394
ΔCDR vs. simplified	—	−6.2%	−10.8%

C Potential geochemical and transport losses

C.1 Geochemical and transport losses

The near-field zone (Table 13) refers to the upper soil column where primary weathering reactions occur, typically defined as 0–20 cm depth or the depth of tillage plus a buffer depth that has yet to be concretely defined. Potential loss estimates drawn from the relevant documentation are indicative ranges; actual losses are highly site-dependent. The far-field zone (Table 14) encompasses the transport pathway from the soil column through groundwater flow paths, river systems and ultimately the ocean. Riverine losses are highly dependent on catchment hydrology, with greater losses in systems where a larger fraction of weathering products enter surface waters. Marine losses reflect thermodynamic constraints on ocean CO_2 uptake capacity. Loss estimates are illustrative ranges. Actual losses vary with environmental conditions.

Table 13: Near-field geochemical losses in enhanced rock weathering carbon accounting.

Loss Mechanism	Description	Potential loss	Sources
Secondary carbonate precipitation	Formation of $CaCO_3$ in soils releases 50% of captured CO_2 per mole precipitated. Favored by high pH, elevated Ca^{2+} and HCO_3^-, limited water movement.	Up to 50% loss per mole precipitated	Dietzen et al. (2018); Renforth (2012); Zamanian et al. (2016); Monger et al. (2015)
Secondary silicate formation	Formation of clay minerals (e.g., kaolinite, smectite) consumes weathering-derived cations and silica, reducing net alkalinity export.	Variable; highly site-dependent	Calabrese et al. (2022); Amann and Hartmann (2022); Dupla et al. (2023); Wild et al. (2024)
Cation exchange and sorption	Net adsorption of base cations (Ca^{2+}, Mg^{2+}) to soil exchange sites. Can be positive (loss) or negative (release from native soil minerals).	Reversible; typically small	Pogge von Strandmann et al. (2023); Kelland et al. (2020); ISO 11260:2018
Plant biomass uptake	Removal of base cations via harvested crops. Annual removal proportional to biomass yield and tissue cation content.	Crop-dependent; 1–15% of weathering flux	Beerling et al. (2020); Taylor et al. (2016); Kantola et al. (2017); Kantola et al. (2023); Amann et al. (2020)
Non-carbonic acid weathering	Weathering driven by HNO_3 (from fertilizer nitrification) or H_2SO_4 (from sulfide oxidation) does not consume atmospheric CO_2.	Up to 30% in synthetic input rich, fertilized systems	Perrin et al. (2008); Hamilton et al. (2007); Semhi et al. (2000); Probst et al. (1994)

Table 14: Far-field transport losses in enhanced rock weathering carbon accounting.

Loss Mechanism	Description	Potential loss	Sources
Riverine CO_2 outgassing	Soil waters with high pCO_2 equilibrate with atmosphere upon entering streams, driving calcite supersaturation and CO_2 evasion.	$\leq$5% (low flux) to 16–27% (high flux)	Zhang et al. (2022); Harrington et al. (2023); Raymond et al. (2013); Lauerwald et al. (2015)
Riverine carbonate precipitation	Calcite precipitation in supersaturated rivers (SI $\gg$ 1.0), releasing CO_2. More likely in catchments with high cropland-to-discharge ratios.	Included in riverine loss estimate	Harrington et al. (2023); Gómez de la Peña et al. (2020); Liu et al. (2011)
Marine CO_2 outgassing	Re-equilibration of dissolved inorganic carbon (DIC) system in ocean; carbonate buffering limits net CO_2 uptake efficiency.	$\sim$10–20% equilibration loss	Renforth and Henderson (2017); Middelburg et al. (2020); Zeebe and Wolf-Gladrow (2001); Bach et al. (2019)

C.2 Near field loss, cation uptake by crops

Although we treat the loss term L generically in the main text, we collected biomass and yield measurements that allow a brief quantification of cation export by crops. The net potential CDR is partially offset by uptake of major cations (Ca, Mg, K) by the crop. Harvested biomass removes base cations from the field that would otherwise contribute to long-term alkalinity export; however, this cation loss represents only ∼3% of gross CDR from weathering (Figure 9, SI C.2). The CDR penalty from cation export in harvested biomass is calculated as:

$$\begin{aligned} \mathrm{CDR}_{\mathrm{loss}} &= (2n_{\mathrm{Ca}} + 2n_{\mathrm{Mg}} + n_{\mathrm{K}}) \times M_{\mathrm{CO_2}} \\ &= \left(\frac{2m_{\mathrm{Ca}}}{M_{\mathrm{Ca}}} + \frac{2m_{\mathrm{Mg}}}{M_{\mathrm{Mg}}} + \frac{m_{\mathrm{K}}}{M_{\mathrm{K}}} \right) \times 44.01 \end{aligned} \tag{26}$$

where $m_i = C_i \times Y$ is the mass of cation i removed in biomass (concentration C_i times yield Y), and M_i is the molar mass. Divalent cations (Ca^{2+}, Mg^{2+}) each balance two moles of bicarbonate alkalinity, while monovalent K^+ balances one.

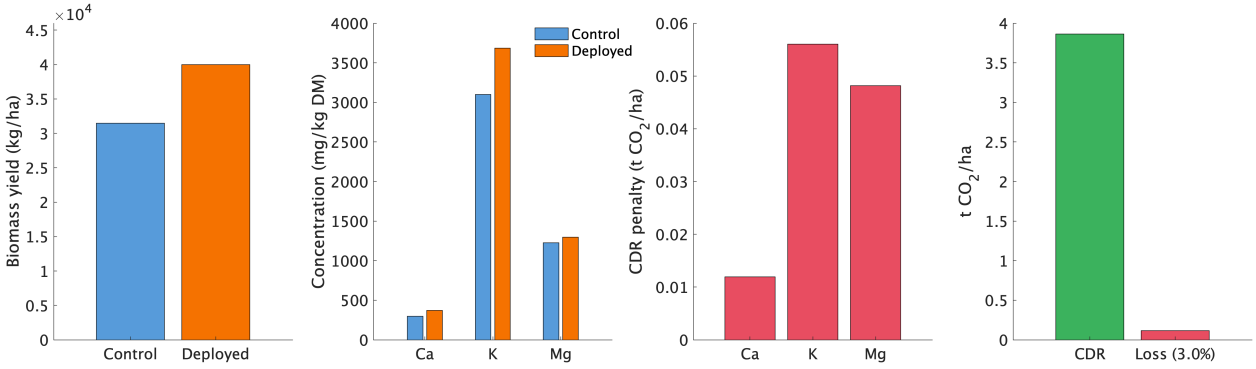

Figure 9: Cation uptake by rice biomass and implications for CDR accounting. (a) Total aboveground biomass yield in control and basalt-deployed plots. (b) Concentrations of Ca, K, and Mg in rice dry matter. (c) CDR penalty associated with cation export in harvested biomass, calculated as the CO_2 equivalence of base cations removed from the field. (d) Comparison of gross CDR from basalt weathering with the cation export loss, showing that biomass removal offsets approximately 3.0% of weathering-derived CDR.